Numerical simulation of gas composition tracking in a gas transportation network

Alfredo Bermúdez [a, b, *], Mohsen Shabani [b]

[a] Departamento de Matemática Aplicada and Instituto de Matemáticas (IMAT), Universidade de Santiago de Compostela, E-15782, Santiago de Compostela, Spain
[b] Instituto Tecnológico de Matemática Industrial (ITMATI), Edif. Instituto Investigaciones Tecnológicas, Planta -1, E-15782, Santiago de Compostela, Spain

ARTICLE INFO

ABSTRACT

In previous papers of the authors, a new formulation for isothermal flow of gas mixtures with given constant composition in a transportation network including usual devices has been introduced and solved. However, in real networks, different gas qualities are introduced from different entry points. In this case, it is important to track the quality along the network over time and therefore a multi-species model has to be used. The main objective of the present paper is to introduce a model allowing us to simulate the evolution of the gas composition, at each point in the network and over time, and then to couple it with the flow model. The model for tracking the gas composition consists of a system of first order partial differential equations, one per pipe and per species, which are coupled together at the nodes by imposing the mass conservation equation for each species. It is important to notice that the coupling condition at the nodes guarantees that the numerical scheme conserves the mass of each species along the time. In order to validate the overall methodology, it is applied to a test case on a real network. Numerical results show good agreement with measurements.

© 2022 The Authors. Published by Elsevier Ltd. This is an open access article under the CC BY-NC-ND license (http://creativecommons.org/licenses/by-nc-nd/4.0/).

1. Introduction

Reducing greenhouse gas emissions is a high priority objective in recent years, as these emissions have a negative impact on climate change. In the year 2020, oil continues to hold the largest share of the energy mix (31.2%). Coal is the second largest, accounting for 27.2% of total primary energy consumption, a slight increase from 27.1% in 2019. The share of both natural gas and renewables rose to record highs of 24.7% and 5.7%, respectively, [1]. The way of energy production is being directed towards reducing the consumption of fossil fuels with the use of clean and renewable energies such as wind and solar energy. The growth of the world capacity to generate electricity from solar panels, wind turbines and other renewable technologies is on course to accelerate over the coming years. Despite rising costs for key materials used to make solar panels and wind turbines, additions of new renewable power capacity are forecast to rise from almost 300 GW in 2021 until around 460 GW in 2026 [2].

Currently, one of the specific decisions under study is to produce hydrogen (perhaps from renewable electricity) as well as biogas, and mix them with natural gas in a proportion to be determined. The resulting mixture would be transported using existing natural gas networks. In these circumstances, the numerical simulation of the composition of the mixture along the networks and, more importantly, at the delivery points, becomes a very helpful tool in the management of gas networks, in particular because the gas is sold for its energy content based on tariff conditions [3] and energy content is directly related to composition [4—7].

In order to calculate the transported energy, several research articles, and some commercial software like OLGA and PIPESIM (Schlumberger company), Synergi Gas modules (DNV company) and PipelineStudio (EMERSON) are being devoted to the simulation of multi-species gas flow in order to track the quality of the gas in terms of gas composition or specific energy. Having good accuracy in gas quality monitoring allows us to increase the reliability of the amount of energy sold and reduce the number of metering devices and their calibration used to calculate the customer's bill [8].

* Corresponding author. Departamento de Matemática Aplicada and Instituto de Matemáticas (IMAT), Universidade de Santiago de Compostela, E-15782, Santiago de Compostela, Spain.
E-mail addresses: alfredo.bermudez@usc.es (A. Bermúdez), shabani.mohsen@outlook.com (M. Shabani).

Nomenclature

FEM	Finite Element Method
FVM	Finite Volume Method
PDAE	Partial Differential-Algebraic Equation
FCV	Flow Control Valve
PCV	Pressure Control Valve
f	frictionfactor
M	number of finite elements
t	time, s
Δt_i	time-step size corresponding to i, s
T	length of the time interval of simulation, s
s	time, s
ρ	density, kg/m^3
ϵ	roughness of pipe, m
u	velocity, m/s
q	mass flow rate per unit area (or mass flux), kg/m^{2}s
F_i	function of time in boundary conditions
p	pressure, Pa
$\mathcal{E}$	specific total energy, J/kg
p_c	critical pressure, Pa
a	isothermal sound speed in gas, m/sec
R	gas constant, J/(kgK)
X_i	molar fraction
$\mathcal{M}_i$	molar mass of i-th species, kg/mol
Q	mass flow rate, kg/s
j	pipe number
A	Incidence matrix
λ_i	Lagrange multiplier corresponding to pressure at node i, Pa
NSE	Number of sub-elemets
η	Viscosity of gas mixture
N	number of Nodes
E	number of Edges
m	connectivity matrix
x	coordinate along the pipe, m
D	diameter, m
L	length of pipe, m
g	gravity acceleration, m/s^2
h	height of the pipe at the x cross-section
ζ	heat transfer coeffient, W/m^{2}K
θ	gas absolute temperature, K
θ_{ext}	exterior temperature, K
Z	compressibility factor
Re	Reynoldsnumber
ρ_{IC}	initial density along the pipe, kg/m^3
q_{IC}	initial mass flux along the pipe, kg/m^{2}s
Q_{IC}	initial mass flow rate along the pipe, kg/s
ψ	test function for the weak formulation
P_l	space of polynomials of degree l
θ_c	critical temperature, K
P_1	space of polynomials of degree one
$\|e\|_1$	L^1 -norm for calculating the errors
α, β, γ	coefficient of time weighted average for time discretization
Y_i	mass fraction
$\mathcal{M}$	molar mas of mixture, kg/mol
Φ	new function which is defined as the integration of Q over the time, kg
S^j	area of the cross-section of the j-th pipe, m^2
$\top$	transposed of a matrix
c^i	emisson or consumption at node i, kg/s
$\chi_{k,n}^i$	k-th species at time step n, and consumption node i
$\iota_{k,n}^i$	k-th species at time step n, and emission node i

These research articles can be classified into several groups. Some authors, as [9,10], derive the governing equations directly in terms of the energy content and use them to simulate steady-state situations.

More recent studies consider a gas mixture with different types of boundary conditions like volumetric flow rate [11–13] or mass flow rate [14,15]. In Refs. [16,17] a mixture including hydrogen is considered. However, in these studies, the gas composition remains constant over time which is not a realistic situation because very often there are several gas inputs with different qualities.

In other papers, as [18–22], the Wobbe index and the calorific value are used to assess the gas quality. However, on the one hand gas quality in the transportation network always changes over time and, on the other hand, the developing and growing gas markets need to simulate gas quality with high precision which, in general, cannot be achieved with traditional methods. Hence, some recent research has been specifically focused on transient models for tracking gas composition [8,23–25] rather than specific energy. In Refs. [8,23], a single pipeline has been modelled and an implicit centered finite difference scheme has been used for numerical solution. In the former, the energy flow was also solved along with the governing model for tracking gas composition while, in the latter, only the gas composition tracking was considered. In Ref. [8], a non-isothermal gas flow model in a pipeline is considered. The species equations are coupled and solved simultaneously with the governing flow equations. The authors considered three examples, two of them are used for validating with field data and assessing the model accuracy, which is affected by the calorific value and the flow rate gradients. The third one illustrates the effect of hydrogen injection in the pipeline. The results show that variable gas quality has a remarkable effect on the pipeline system. They highlight that the operation of power to gas (P2G) plants, the natural gas scheduling, and the operational planning of the transmission systems should be considered as a single unit. Consequently, all kind of energy introduced into transmission systems is expected to be synchronized with other sectors. However, they returned to the traditional way of tracking the gas composition and, in Ref. [23], two different methods are compared. The first one is a moving grid method (batch tracking), and the second one is an implicit backward difference method. These methods were applied to simulate an onshore Polish and an offshore Norwegian gas transportation pipes. The differences between the simulated and measured compositions were studied. The errors were less than 2.0% and were sensitive to flow variations. The results illustrate that, unlike the moving grid method which conserves the shape of the composition variation, the implicit method loses some of the finer details of tracked gas composition because of numerical diffusion. It should be mentioned that in the batch tracking method, only one-direction gas flow is considered along each pipe. Hence, those cases where the velocity may have different signs in the same pipe cannot be

solved. However, in the present study, thanks to the use of the method of characteristic we have avoided this limitation as the flow direction can change inside a pipe. They also stated that the difference in simulation time between the two gas tracking methods is small. Furthermore, in the aforementioned onshore pipeline, a comparison of the calculation time between simulating or not simulating the gas composition shows a difference of the order of 20%. We also note that neither of these two studies is used to track gas composition in a full network.

In [24], numerical simulation of transient composition was developed for non-isothermal natural gas transmission networks. Flow and composition tracking were solved separately by an explicit first-order upwind finite volume scheme. The solution procedure includes three steps: transient flow simulation, transient composition simulation, and calculation of quality parameters. To validate and show the performance of their method, the authors solved several cases including blending a small amount of hydrogen (under 3% mass fraction) into natural gas. Comparison of their results with measurements showed good agreement. They mentioned that the gas composition tracking is a very difficult problem and that up to now the variation of natural gas quality is represented by higher calorific value (HCV) and Wobbe index. Hence, they also present their results in these parameters. Unlike that study, in the present paper we have tracked the gas composition over time and our tests compare this composition (in terms of mass fraction of species) with measurements. In addition, they also stated that blending hydrogen in natural gas inside a network is a complicated issue and that their method should be used carefully. On the other hand, it should also be mentioned that their method produces quite numerical diffusion [26].

Finally, in Ref. [25], the full multi-species Euler equations are solved by using finite volume discretizations and approximate Riemann solvers. While numerical results clearly show first order of accuracy and good stability properties, mass is not exactly conserved; instead its conservation is only achieved up to the first order of accuracy.

In previous papers, the authors have introduced and then solved by using finite element methods, a new formulation for isothermal gas flow in transportation networks [27,28], including usual devices as compressors or valves, [29]. In these papers, a given uniform composition of the gas has been assumed. Thus, going a step further, the main objective of the present paper is to deal with the more general case in which the gas has a variable composition throughout the network and over time. This makes it necessary to couple the flow equations with the transport equations for species. The whole model would allow us to track the composition of gas in a real transportation network involving different qualities of gas.

For the numerical solution, unlike what is done in most papers on the subject (an exception is the recent and interesting reference [24] cited above), we propose a segregated method solving the gas flow equations and the species transport equations separately. We note that this way of solving the complete model allows us to consider different numerical methods and also different meshes to solve each of the two sets of governing equations. In doing so, a high precision in the numerical solution has been achieved by choosing a second order finite element method for the flow equations on a coarse mesh and a first order characteristics method for the species equation on a finer mesh. This strategy enable us to obtain accurate results for the gas species equation without significantly increasing the overall computational cost, as we use a coarser mesh to solve the flow equations, which are the most expensive part of the model. It should be noted that the method of characteristics exhibits less diffusion compared to other upwind methods [24]. as mentioned, for instance, in Ref. [26].

Importantly, as we have previously shown in Ref. [28], our proposed finite element method for the flow equations conserves exactly the mass of the total gas mixture at the nodes of the network in the case of uniform gas composition. Similarly, the method proposed in the present paper has the interesting property of conserving the mass of each species at the discrete level. We emphasize that the importance of mass conservation becomes apparent, for instance, when it is needed to compute the line-pack (i.e., the total energy of the gas contained in the whole network at any particular time) or the amount of energy sold at the delivery nodes of the network.

Another practical interesting feature of our method is the following. We have compared the results obtained when the gas properties that depend on composition are updated in the flow equation at every time step in two different ways: from the composition at each mesh point of the pipe, or from the average composition throughout the whole pipe. In real cases, both results are similar but the second choice significantly reduces the computing time. Thus, the proposed method enables long-term simulations of real gas networks in a short time, which opens the door to solve practical problems of control and dynamic optimization.

The outline of the paper is as follows. In Section 2, the full mathematical model for multi-species gas flow in a pipe is described. In Subsection 2.1 the governing flow equations for a pipe are simplified from several assumptions and these simplified equations are then rewritten in an equivalent form involving only one equation with an unknown function. Also, some closure relations for the model are defined in Subsection 2.2. The model for the flow throughout the transmission network is recalled in Section 3 after which the model for gas composition tracking is introduced. In Section 4, numerical methods for solving flow and species equations are given and then some related issues are discussed. The last Section 5 is devoted to presenting numerical results for two test problems: the first is a non-trivial fairly standard academic test on the species transport equation. The second deals with a small real network for which experimental measurements are available. Both tests allow us to validate the methodology. Finally, some conclusions are drawn from the present study. A research flow chart of the present study is shown in Fig. 1.

2. Modelling multi-species gas flow in a pipe

2.1. Governing equations

The dynamic behavior of gas flow in a pipe as shown in Fig. 2 can be described by the standard compressible Euler equations with some additional terms to model viscous friction and gravity force (see, for instance Ref. [30]).

Moreover, if we are concerned with the transport of a physical quantity like the gas composition (e.g., the mass fraction of species), the one-dimensional transport equation must be solved in addition
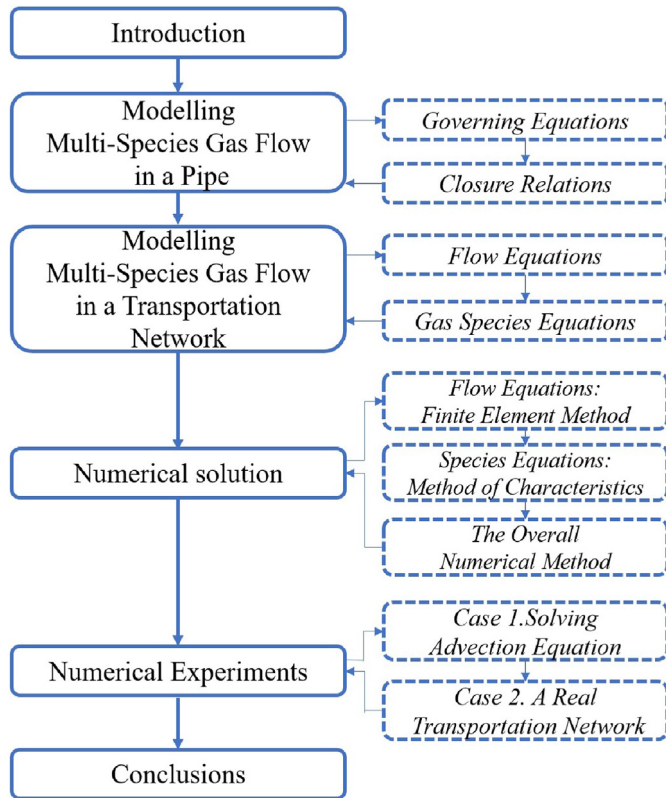
Fig. 1. Research flow chart of the present study.

to the governing flow equations [23,24,29]. Summarizing, the whole model to simulate multi-species flow in a pipe consists of the system of partial differential equations (1)–(4) and equation of state (5) below:

$$\frac{\partial \rho}{\partial t}(x,t) + \frac{\partial(\rho u)}{\partial x}(x,t) = 0, \tag{1}$$

$$\frac{\partial(\rho u)}{\partial t}(x,t) + \frac{\partial\left(\rho u^2 + p\right)}{\partial x}(x,t) = -\frac{f}{2D}\rho(x,t)u(x,t)\,u(x,t) - g\rho(x,t)\frac{dh}{dx}(x) \tag{2}$$

$$\frac{\partial(\rho E)}{\partial t}(x,t) + \frac{\partial((\rho E + p)u)}{\partial x}(x,t) = -\frac{4\zeta}{2D}\left(\theta_{ext}(x,t) - \theta(x,t)\right) - g\rho(x,t)u(x,t)\frac{dh}{dx}(x), \tag{3}$$

$$\frac{\partial(\rho Y_k)}{\partial t} + \frac{\partial(\rho Y_k u)}{\partial x} = 0, \ k = 1,\ldots,N_c. \tag{4}$$

$$p = Z(p,\theta)\rho R\theta, \tag{5}$$

where in equations (1) and (2), ρ, u, p are mass density, mass-averaged axial velocity, and pressure, respectively. Besides, g is the gravity acceleration, D is the diameter of the pipe, and f is the friction factor on the wall. Fields E, θ, and ζ in equation (3) refer to specific total energy, absolute temperature and heat transfer coefficient, respectively. Mass fraction of the k-th species is denoted by Y_k. Finally, in the equation of state (5), Z is the compressibility factor.

Usually, some reasonable assumptions have been considered in the simulation of real gas networks [27,31–40]. In the present study, the two following ones are chosen:

H1. The gas temperature along the pipe as a function of x and t is known so the energy equation is not needed.

H2. The convective term is neglected in the momentum equation. This can be done as far as the Mach number is small, which is a plausible assumption in gas transportation networks.

From these assumptions, equations (1)–(3) can be simplified to (see Refs. [27–29]),

$$\rho_t(x,t) + q_x(x,t) = 0, \tag{6}$$

$$q_t(x,t) + \left(a^2(x,t)\rho(x,t)\right)_x + \frac{f\left(\text{Re}(x,t),\frac{\epsilon}{D}\right)}{2D}\frac{q(x,t)q(x,t)}{\rho(x,t)}$$
$$+ \rho(x,t)gh_x$$
$$= 0 \tag{7}$$

where $q = \rho u$ is the mass flux (kg/(m^2 s)) and the other notations have been previously established. Function $a\,(x,t)$ is defined by

$$a(x,t) := \sqrt{Z(p(x,t),\theta(x,t))R\theta(x,t)} \ \ (\text{m/s}). \tag{8}$$

Now, by introducing a new unknown as proposed in Ref. [27], namely,

$$\Phi^j(x,t) = \int_0^t Q^j(x,s)ds, \tag{9}$$

where $Q^j\,(x,s) := S^j q^j\,(x,s)$ is the mass flow rate (kg/s) at the cross-section of the j-th pipe located at x and at time t, the above equations can be rewritten as a single second-order partial differential equation in time and space:
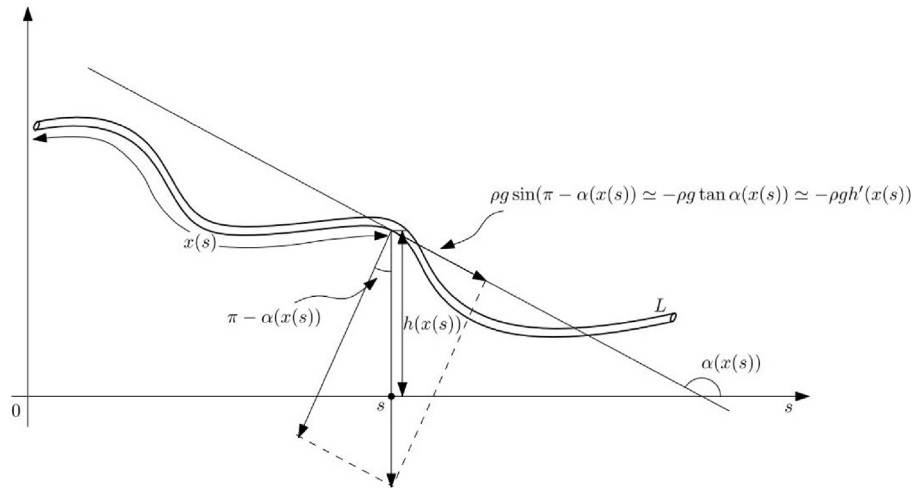
Fig. 2. Geometry and approximation of gravity term.

$$\frac{1}{S^j}\Phi^j_{tt}(x,t) - \frac{1}{S^j}\left(\left(a^j\right)^2(x,t)\Phi^j_x(x,t)\right)_x(x,t)$$

$$+ \frac{f\left(\mathrm{Re}^j(x,t),\dfrac{e^j}{D^j}\right)}{2D^j}\frac{1}{S^j}\frac{\Phi^j_t(x,t)\Phi^j_t(x,t)}{S^j\rho^j_{IC}(x) - \Phi^j_x(x,t)}$$

$$-\frac{1}{S^j}g\Phi^j_x(x,t)h^j_x = -\rho^j_{IC}(x)gh^j_x$$

$$-\left(\left(a^j\right)^2(x,t)\rho^j_{IC}(x)\right)_x.$$

(10)

We notice that this formulation only includes one unknown function per pipe, namely $\Phi^j(x,t)$, from which the primitive physical magnitudes, that is, density, pressure, and gas velocity can be easily computed by post-processing this function (see again [27]).

2.2. Closure relations

In order to solve the above equations, some additional information is needed. It consists of four so-called *closure relations*:

CR1. The compressibility factor of real gas is computed by using the Papay's formula [41]:

$$Z(p,\theta) = 1 - 3.52p_r e^{-2.26\,\theta_r} + 0.274p_r^2 e^{-1.878\,\theta_r}$$

(11)

where p_r and θ_r are the reduced pressure and temperature, respectively, that is,

$$p_r = \frac{p}{p_c}, \quad \theta_r = \frac{\theta}{\theta_c},$$

being p_c the critical pressure and θ_c the critical temperature of the gas which depend upon composition through the *Kay's formulas*,

$$\theta_c = \sum_{i=1}^{N_c} X_i \theta_{c,i}, \quad p_c = \sum_{i=1}^{N_c} X_i p_{c,i}.$$

In these formulas, X_i denotes the molar fraction of the *i*-th species of the gas mixture and $\theta_{c,i}$ and $p_{c,i}$ are its critical temperature and pressure, respectively. Let us recall that

$$X_i = \frac{\mathcal{M}}{\mathcal{M}_i}Y_i, \ i = 1, \ldots, N_c,$$

where $\mathcal{M}$ is the molar mass (kg/mol) of the gas mixture and $\mathcal{M}_i$ is the molar mass of the *i*-th species. We recall that $\mathcal{M}$ depends on the gas composition through the formula

$$\mathcal{M} = \left(\sum_{i=1}^{N_c}\frac{Y_i}{\mathcal{M}_i}\right)^{-1}.$$

CR2. The friction factor is obtained from the roughness of the pipe ϵ and the Reynolds number by using, for instance, the following formula (see Ref. [42]):

$$f = 1.613\left[\ln\left(0.234\left(\frac{\epsilon}{D}\right)^{1.100\,7} - \frac{60.525}{\mathrm{Re}^{1.110\,5}} + \frac{56.291}{\mathrm{Re}^{1.071\,2}}\right)\right]^{-2},$$

(12)

where, as usual, the Reynolds number is defined as

$$\text{Re} = \frac{\rho u D}{\eta}.$$

CR3. The dynamic viscosity of the gas is a function of temperature and density (or pressure) which, in turn, depends on gas composition. The Yang's relation [43] is used to calculate the gas viscosity:

$$\eta = \eta_B \sqrt{\theta_r} \exp\left(\frac{\varpi + (A_b + A_k \theta_r)\rho_r^\omega}{\theta_r}\right), \tag{13}$$

where

$$\eta_B = B\mathcal{M}_{sqrt} \quad \text{and} \quad \mathcal{M}_{sqrt} = \sum_{i=1}^{N_c} X_i \sqrt{\mathcal{M}_i},$$

being θ_r and ρ_r the reduced temperature and density, respectively. The other parameters are $B = 3.142$, $\varpi = -0.551$, $A_k = 0.172$, $A_b = 0.621$ and $\omega = 1.273$.

CR4. Finally, R is the specific gas constant, that is, $R = \frac{\mathcal{R}}{\mathcal{M}}$, being $\mathcal{R} = 8.314$ J/(K mol) the universal gas constant.

3. Modelling multi-species gas flow in a transportation network

3.1. The flow equations

In this section, the topology of the gas network is taken into account by using a directed graph with N nodes and E edges. We recall the definition of the incidence matrix, $A = (a_{ij})$ (see, for instance Ref. [28]):

$$a_{ij} = \begin{cases} +1 & \text{if node } i \text{ is the first node of edge } j \\ -1 & \text{if node } i \text{ is the second node of edge } j \\ 0 & \text{otherwise} \end{cases}$$

where $i = 1, ..., N$ and $j = 1, ..., E$.

By splitting the incidence matrix A into its positive and negative parts, $A = A^+ - A^-$, the total mass conservation at the i-th node can be written as

$$\sum_{j=1}^{E} a_{ij}^+ Q^j(0, t) - \sum_{j=1}^{E} a_{ij}^- Q^j(L^j, t) = c_i(t), \quad i = 1, ..., N, \tag{14}$$

where $c_i(t)$ denotes the exchanged mass flow rate (kg/s) with the exterior of the network at the i-th node. For the sake of simplicity and compactness in notation, the mass conservation at nodes (14) is rewritten in vector form,

$$A^+ \mathbf{Q}(0, t) - A^- \mathbf{Q}(L, t) = \mathbf{c}(t), \tag{15}$$

where $\mathbf{Q}$ denotes the E-dimensional vector with components Q^j.

The mass conservation equations at nodes will be called *first*

kind nodal boundary conditions. The vector of nodal pressures (notice that pressure is a common magnitude for all edges meeting at each particular node) will be denoted by $\lambda(t) \in \mathbb{R}^N$ and called the *second kind nodal boundary conditions*. By using the incidence matrix we can write

$$\mathbf{p}(0, t) = (A^+)^\top \lambda(t), \tag{16}$$

$$\mathbf{p}(L, t) = (A^-)^\top \lambda(t) \tag{17}$$

and also,

$$\lambda(t) = B^{-1}(A^+ \mathbf{p}(0, t) + A^- \mathbf{p}(L, t)), \tag{18}$$

where B is a diagonal matrix giving the number of pipes that join at the i-th node:

$$B_{ii} := \left(\left|A|\mathbf{e}^E\right)\right._i, \quad i = 1, ..., N,$$

with $|A| = A^+ + A^-$.

We notice that either pressure, $\lambda_i(t)$, or mass flow rate exchanged with the exterior, $c_i(t)$, must be given as nodal boundary data at each node i.

In order to solve the system of one-dimensional nonlinear wave-like equation (10), together with the above defined nodal boundary conditions, a finite element method has been introduced in Ref. [28].

Remark 3.1. Let us notice that, after solving equations (10) with the nodal boundary conditions, the physical magnitudes of interest, namely, density, pressure and mass flow rate can be computed (see Ref. [27]) after which the velocity is obtained as

$$u(x, t) = \frac{q(x, t)}{\rho(x, t)}. \tag{19}$$

3.2. The gas species equations

In order to compute the gas composition along the network, equation (4) have to be solved for all edges together with initial and boundary conditions. Since they are first order equations, a boundary condition is needed only at input flow nodes of the edge, i.e., at $x = 0$, if $Q^j(0, t) > 0$ and at $x = L^j$ if $Q^j(L^j, t) < 0$. Moreover, at each node several pipes may meet. At any time t, some of them transport incoming flow to the node and the rest of them transport outgoing flow from the node. It is assumed that, at any time t, an instantaneous perfect mixing of the incoming flows at the node takes place in such a way that the gas composition is the same for all the outgoing pipes from the node. Let us denote by $\chi_k^i(t)$ the mass fraction of the k-th species leaving node i at time t. Then, we need to solve the following initial-boundary value problems:

$$\frac{\partial\left(\rho^j Y_k^j\right)}{\partial t} + \frac{\partial\left(\rho^j u^j Y_k^j\right)}{\partial x} = 0, \quad (x, t) \in \left[0, L^j\right] \times [0, T], \tag{20}$$

$$Y_k^j(x, 0) = Y_{k,IC}^j(x), \quad x \in \left[0, L^j\right], \tag{21}$$

$$Y_k^j(0, t) = ((A^+)^\top \chi_k(t))_j, \quad t \in [0, T], \text{ if } Q^j(0, t) > 0 \tag{22}$$

and
$$Y_k^j(L^j, t) = ((A^-)^\top \chi_k(t))_j, \quad t \in [0, T], \text{ if } Q^j(L^j, t) < 0, \tag{23}$$

where $\chi_k(t) = \left(\chi_k^1(t), ..., \chi_k^N(t)\right)^\top$.

We notice that, by using the total mass conservation equation (6), it can be easily seen that equation (20) can be written in their (equivalent) non-conservative forms,

$$\frac{\partial Y_k^j}{\partial t} + u^j \frac{\partial Y_k^j}{\partial x} = 0, \quad (x, t) \in [0, L^j] \times [0, T], \tag{24}$$

which are the ones we are going to solve numerically.

In addition to equation (14) for total mass conservation at the nodes, we need to include the mass conservation equations for each species, to be called the *third kind nodal boundary conditions*. These boundary conditions will allow us to compute the mass fraction of the k-th species leaving node i at time t, that is, the unknowns $\chi_k^i(t)$ previously introduced. Notice that, if the flow exchanged with the exterior of the network through node i at time t, $c^i(t)$, is positive (i.e., the gas enters the network from outside), then the composition of this incoming gas must be given as a *nodal data of the third kind*: let us denote by $\iota_k^i(t)$ the mass fraction of the k-th species. Then, for $i = 1, ..., N$ we have either

$$+ \sum_{j=1}^E A_{ij}^+ \left(\left(Q^j(0, t)\right)^+ \chi_k^i(t) - \left(Q^j(0, t)\right)^- Y_k^j(0, t) \right)$$

$$- \sum_{j=1}^E A_{ij}^- \left(\left(Q^j\left(L^j, t\right)\right)^+ Y_k^j\left(L^j, t\right) - \left(Q^j\left(L^j, t\right)\right)^- \chi_k^i(t) \right)$$

$$= c^i(t)\iota_k^i(t), \quad \text{if } c^i(t) > 0 \left(\text{emission node}\right)$$

or

$$+ \sum_{j=1}^E A_{ij}^+ \left(\left(Q^j(0, t)\right)^+ \chi_k^i(t) - \left(Q^j(0, t)\right)^- Y_k^j(0, t) \right)$$

$$- \sum_{j=1}^E A_{ij}^- \left(\left(Q^j\left(L^j, t\right)\right)^+ Y_k^j\left(L^j, t\right) - \left(Q^j\left(L^j, t\right)\right)^- \chi_k^i(t) \right)$$

$$= c^i(t)\chi_k^i(t), \quad \text{if } c^i(t) < 0 \text{ (consumption node)}.$$

Let us also recall that, by definition of Φ^j, the mass flow rates at the ends of the j-th pipe are given by

$$Q^j(0, t) = \Phi_t^j(0, t) \text{ and } Q^j\left(L^j, t\right) = \Phi_t^j\left(L^j, t\right).$$

Therefore, the above equations can also be written as

$$+ \sum_{j=1}^E A_{ij}^+ \left(\left(\Phi_t^j(0, t)\right)^+ \chi_k^i(t) - \left(\Phi_t^j(0, t)\right)^- Y_k^j(0, t) \right)$$

$$- \sum_{j=1}^E A_{ij}^- \left(\left(\Phi_t^j\left(L^j, t\right)\right)^+ Y_k^j\left(L^j, t\right) - \left(\Phi_t^j\left(L^j, t\right)\right)^- \chi_k^i(t) \right) \tag{25}$$

$$= c^i(t)\iota_k^i(t), \quad \text{if } c^i(t) > 0 \text{ (emission node)},$$

or

$$+ \sum_{j=1}^E A_{ij}^+ \left(\left(\Phi_t^j(0, t)\right)^+ \chi_k^i(t) - \left(\Phi_t^j(0, t)\right)^- Y_k^j(0, t) \right)$$

$$- \sum_{j=1}^E A_{ij}^- \left(\left(\Phi_t^j\left(L^j, t\right)\right)^+ Y_k^j\left(L^j, t\right) - \left(\Phi_t^j\left(L^j, t\right)\right)^- \chi_k^i(t) \right) \tag{26}$$

$$= c^i(t)\chi_k^i(t), \quad \text{if } c^i(t) < 0 \text{ (consumption node)}$$

4. Numerical solution

4.1. Flow equations: finite element method

In this subsection, we shortly summarize the methods introduced in Ref. [28] for the numerical solution of the flow equations. Firstly, let us introduce a mesh of the time interval $[0, T]$. Given a natural number M, let $0 = t_0 < t_1 < ... < t_M$, with $t_n = n\Delta t, n = 0, ...M$ and $\Delta t = T/M$.

The time derivatives of Φ^j are approximated by second-order central difference formulas while their first derivatives with respect to x are computed from a weighted average involving the values of Φ^j at three consecutive time steps, with weights α, β and γ. With the aim of having second-order of accuracy both in time and in space, α and γ should be chosen to have the same value. In particular, by taking $\alpha = \gamma = 0.25$ and $\beta = 0.5$ the method will be stable for linear problems independently of Δt and the truncation error will be minimized (see Ref. [44]). The weak formulation of the semi-discrete in time approximate problem is the following (see Ref. [28] for further details):

At step $n \in \{0, ..., M - 1\}$, we compute approximations of $\mathbf{\Phi}(x, t_{n+1})$ and $\lambda^F(t_{n+1})$, to be called $\mathbf{\Phi}_{n+1}(x)$ and λ_{n+1}^F, satisfying

for all $\psi^j, j = 1, ..., P$ and $\mathbf{w}^F \in \mathbb{R}^F$, with

$$\sum_{j=1}^{E} \int_{0}^{L^j} \frac{1}{S^j} \frac{\Phi_{n+1}^j(x) - 2\Phi_n^j(x) + \Phi_{n-1}^j(x)}{\Delta t^2} \psi^j(x) dx$$

$$+ \sum_{j=1}^{E} \int_{0}^{L^j} \frac{1}{S^j} \left(a^j\right)_n^2(x) \frac{d}{dx} \left[\frac{\alpha \Phi_{n+1}^j(x) + \beta \Phi_n^j(x) + \gamma \Phi_{n-1}^j(x)}{\alpha + \beta + \gamma} \right] \psi_x^j(x) dx$$

$$+ \sum_{j=1}^{E} \int_{0}^{L^j} \frac{f_n^j(x)}{2D^j} \frac{1}{S^j} \frac{\dfrac{\Phi_{n+1}^j(x) - \Phi_{n-1}^j(x)}{2\Delta t} \dfrac{\Phi_{n+1}^j(x) - \Phi_{n-1}^j(x)}{2\Delta t}}{\rho_{IC}^j(x) S^j - \dfrac{d}{dx}\left[\dfrac{\alpha \Phi_{n+1}^j(x) + \beta \Phi_n^j(x) + \gamma \Phi_{n-1}^j(x)}{\alpha + \beta + \gamma}\right]} \psi^j(x) dx \qquad (27)$$

$$- \sum_{j=1}^{E} \int_{0}^{L^j} \frac{1}{S^j} \frac{d}{dx} \left[\frac{\alpha \Phi_{n+1}^j(x) + \beta \Phi_n^j(x) + \gamma \Phi_{n-1}^j(x)}{\alpha + \beta + \gamma} \right] g h^j(x) \psi^j(x) dx$$

$$= - \sum_{j=1}^{E} \int_{0}^{L^j} \rho_{IC}^j(x) g h_x^j(x) \psi(x) dx + \sum_{j=1}^{E} \int_{0}^{L^j} \left(a^j\right)_n^2(x) \rho_{IC}^j(x) \psi_x^j(x) dx$$

$$+ \lambda^P(t_n) \cdot \mathcal{P}(A^+ \psi(0) - A^- \psi(\mathbf{L})) + \left(\alpha \lambda_{n+1}^F + \beta \lambda_n^F + \gamma \lambda_{n-1}^F\right) \cdot \mathcal{F}(A^+ \psi(0) - A^- \psi(\mathbf{L})),$$

$$\mathcal{F}\left(A^+ \left(\frac{\Phi_{n+1}(0) - \Phi_{n-1}(0)}{2\Delta t}\right) - A^- \left(\frac{\Phi_{n+1}(\mathbf{L}) - \Phi_{n-1}(\mathbf{L})}{2\Delta t}\right)\right) \cdot \mathbf{w}^F = \mathbf{c}^F(t_n) \cdot \mathbf{w}^F, \qquad (28)$$

$$a_n^j(x) = \sqrt{Z\left(p_n^j(x), \theta^j(x, t_n)\right) R_n^j(x) \theta^j(x, t_n)}, \qquad (29)$$

where

$$R_n^j(x) = \frac{\mathcal{R}}{\mathcal{M}_n^j(x)}, \quad \text{with} \quad \frac{1}{\mathcal{M}_n^j(x)} = \sum_{i=1}^{N_c} \frac{Y_n^j(x)}{\mathcal{M}_i},$$

and $p_n^j(x)$ is the solution of the non-linear numerical equation

$$p_n^j(x) = Z\left(p_n^j(x), \theta^j(x, t_n)\right) \rho_n^j(x) R_n^j(x) \theta^j(x, t_n), \quad x \in [0, L^j], \qquad (30)$$

being

$$\rho_n^j(x) = \rho_{IC}^j(x) - \frac{1}{S^j} \Phi_{n,x}^j(x).$$

The last equation comes from the definition of the new unknown Φ^j. Moreover, we notice that, if Papay's formula (11) is used for Z then (30) is a polynomial equation of second degree. Hence, $p_n^j(x)$ can be computed by a simple explicit formula before starting step n, since Φ_n is known from the previous time step. Then, $(a^j)_n^2(x)$ is calculated from (29).

We also notice that step number n runs from $n = 0$ to $M - 1$, where $t_M = T$. For $n = 0$ we need two initial conditions: Φ_0 and Φ_{-1}, which are defined by

$$\Phi_0 = \mathbf{0} \quad \text{and} \quad \Phi_{-1} = \Phi_1 - 2\Delta t \mathbf{Q}_{IC}, \qquad (31)$$

with $Q_{IC}^j = S^j q_{IC}^j$, and λ_0^F, λ_{-1}^F given, respectively, by (see (18))

$$\lambda_0^F := \left(C^{-1}(A^+ \mathbf{p}_{IC}(0) + A^- \mathbf{p}_{IC}(\mathbf{L}))\right) \qquad (32)$$

and

$$\lambda_{-1}^F := \left(C^{-1}(A^+ \mathbf{p}_{-1}(0) + A^- \mathbf{p}_{-1}(\mathbf{L}))\right). \qquad (33)$$

In order to solve the semidiscrete problem (27),(28), a finite element method has been introduced in Ref. [28]. Thus, the problem becomes equivalent to a finite-dimensional system of nonlinear equations that can be solved by using iterative Newton-like methods. As usual, the numerical solution of the full discretized problem will be denoted by $\Phi_{n,h}^j$, where h denotes the spatial mesh-size.

Remark 4.1. Notice that, after solving the previous discrete problem, approximations of the physical magnitudes of interest can be obtained. Firstly, density and mass flow rate are computed by

$$\rho_{n,h}^j = \rho_{IC} - \frac{1}{S} \frac{d}{dx} \left[\frac{\alpha \Phi_{n+1,h}^j + \beta \Phi_{n,h}^j + \gamma \Phi_{n-1,h}^j}{\alpha + \beta + \gamma} \right], \qquad (34)$$

$$q_{n,h}^j = \frac{1}{S} \frac{\Phi_{n+1,h} - \Phi_{n-1,h}}{2\Delta t}, \qquad (35)$$

and then velocity by

$$u_{n,h}^j = \frac{q_{n,h}}{\rho_{n,h}}. \tag{36}$$

It is worth noticing that this velocity field is, in general, a globally discontinuous function that is rational on each interval of the finite element mesh. In particular, if the polynomial degree of the finite element space is one, then $u_{n,h}^j$ is a globally discontinuous piecewise linear function along pipe number j, because density $\rho_{n,h}$ is piecewise constant.

4.2. Species equations: method of characteristics

Each time step of the numerical method consists of two stages. The first one has been described above. Its goal is to compute finite element approximations of functions $\Phi_{n+1}^j(x)$ and then, as a post-processing, to get approximations of density, mass flow rate, velocity, and pressure, at time t_n. In particular, after this first stage we know the velocity at time t_n given by (36).

The second stage consists in the computation of the mass fractions of species at time t_{n+1}, namely, $Y_{k,n+1}^j$, $k = 1, ..., N_c$. For this purpose a full discretization (in time and in space) of (20)-(23) has to be introduced. We emphasize that the spatial mesh to solve these equations needs not to be the same as the finite element mesh for the flow equations. In practice, the latter will be much coarser than the former.

We also need to compute the *outgoing* mass fractions of the k-th component at the i-th node, χ_k^i, $i = 1, ..., N$, $k = 1, ..., N_c$, involved in (20)-(23), by including discrete approximations of equations (25) and (26) into the system, namely.

- if $c^i(t_n) > 0$ (emission node)

$$\chi_{k,n}^i \sum_{j=1}^E A_{ij}^+ \left(\Phi_{n+1}^j(0) - \Phi_{n-1}^j(0) \right)^+ \\ - \sum_{j=1}^E A_{ij}^+ \left(\Phi_{n+1}^j(0) - \Phi_{n-1}^j(0) \right)^- Y_{k,n}^j(0) \\ - \sum_{j=1}^E A_{ij}^- \left(\Phi_{n+1}^j\left(L^j\right) - \Phi_{n-1}^j\left(L^j\right) \right)^+ Y_{k,n}^j\left(L^j\right) \\ + \chi_{k,n}^i \sum_{j=1}^E A_{ij}^- \left(\Phi_{n+1}^j\left(L^j\right) - \Phi_{n-1}^j\left(L^j\right) \right)^- = 2\Delta t c^i(t_n) \iota_{k,n}^i, \tag{37}$$

- if $c^i(t_n) < 0$ (consumption node)

$$\chi_{k,n}^i \sum_{j=1}^E A_{ij}^+ \left(\Phi_{n+1}^j(0) - \Phi_{n-1}^j(0) \right)^+ \\ - \sum_{j=1}^E A_{ij}^+ \left(\Phi_{n+1}^j(0) - \Phi_{n-1}^j(0) \right)^- Y_{k,n}^j(0) \\ - \sum_{j=1}^E A_{ij}^- \left(\Phi_{n+1}^j\left(L^j\right) - \Phi_{n-1}^j\left(L^j\right) \right)^+ Y_{k,n}^j\left(L^j\right) \\ + \chi_{k,n}^i \sum_{j=1}^E A_{ij}^- \left(\Phi_{n+1}^j\left(L^j\right) - \Phi_{n-1}^j\left(L^j\right) \right)^- = 2\Delta t c^i(t_n) \chi_{k,n}^i, \tag{38}$$

where $i = 1, ..., N$.

We notice that, in both cases, the *third kind nodal boundary condition* can be easily obtained. Indeed.

- if $c^i(t_n) > 0$ (emission node)

$$\chi_{k,n}^i = \left(\sum_{j=1}^E A_{ij}^+ \left(\Phi_{n+1}^j(0) - \Phi_{n-1}^j(0) \right)^+ + \sum_{j=1}^E A_{ij}^- \left(\Phi_{n+1}^j\left(L^j\right) - \Phi_{n-1}^j\left(L^j\right) \right)^- \right)^{-1} \\ \times \left(\sum_{j=1}^E A_{ij}^+ \left(\Phi_{n+1}^j(0) - \Phi_{n-1}^j(0) \right)^- Y_{k,n}^j(0) + \sum_{j=1}^E A_{ij}^- \left(\Phi_{n+1}^j\left(L^j\right) - \Phi_{n-1}^j\left(L^j\right) \right)^+ Y_{k,n}^j\left(L^j\right) + 2\Delta t c^i(t_n) \iota_{k,n}^i \right), \quad i = 1, ..., N, \tag{39}$$

- if $c^i(t_n) < 0$ (consumption node)

$$\chi_{k,n}^i = \left(\sum_{j=1}^E A_{ij}^+ \left(\Phi_{n+1}^j(0) - \Phi_{n-1}^j(0) \right)^+ + \sum_{j=1}^E A_{ij}^- \left(\Phi_{n+1}^j\left(L^j\right) - \Phi_{n-1}^j\left(L^j\right) \right)^- - 2\Delta t c^i(t_n) \right)^{-1} \\ \times \left(\sum_{j=1}^E A_{ij}^+ \left(\Phi_{n+1}^j(0) - \Phi_{n-1}^j(0) \right)^- Y_{k,n}^j(0) + \sum_{j=1}^E A_{ij}^- \left(\Phi_{n+1}^j\left(L^j\right) - \Phi_{n-1}^j\left(L^j\right) \right)^+ Y_{k,n}^j\left(L^j\right) \right), \quad i = 1, ..., N. \tag{40}$$

The two cases (39) and (40) can be summarized in the following equation:

$$
\begin{aligned}
\chi_{k,n}^i = &\left(\sum_{j=1}^{E} A_{ij}^+ \left(\Phi_{n+1}^j(0) - \Phi_{n-1}^j(0) \right)^+ + \sum_{j=1}^{E} A_{ij}^- \left(\Phi_{n+1}^j(L^j) - \Phi_{n-1}^j(L^j) \right)^- - 2\Delta t c^i(t_n)(1-\xi) \right)^{-1} \\
&\times \left(\sum_{j=1}^{E} A_{ij}^+ \left(\Phi_{n+1}^j(0) - \Phi_{n-1}^j(0) \right)^- Y_{k,n}^j(0) + \sum_{j=1}^{E} A_{ij}^- \left(\Phi_{n+1}^j(L^j) - \Phi_{n-1}^j(L^j) \right)^+ Y_{k,n}^j(L^j) + 2\Delta t c^i(t_n) \iota_{k,n}^i \xi \right) \, i = 1, \ldots, N,
\end{aligned}
$$

(41)

where.
$$
\xi = \begin{cases} 1 & \text{if } c^i(t_n) > 0 \quad \text{(emission node)}, \\ 0 & \text{if } c^i(t_n) < 0 \quad \text{(consumption node)}. \end{cases}
$$

Notice that, in the previous equation, the term under the inverse represents the sum of the outgoing mass flow rates from the i-th node. If this number was null, the above computations could not be done. Let us analyze this case. Firstly, we observe that this number is non-negative because all of the terms involved in the sum are non-negative. As a consequence, it can be null if and only if all of them are null. From the mass conservation equation, we easily deduce that the i-th node has to be a stagnation point of the flow at the considered time t_n. In particular, $c^i(t_n)$ has to be null and hence the described situation is incompatible with either a non-null consumption or a non-null emission, which is intuitive.

Now, a numerical scheme to solve the mass conservation equations of species is introduced. Firstly, the finite element mesh of the j-th pipe used to solve the flow equations is considered. Denote by x_m^j, $m = 0, \ldots, NSE_j$ the mesh points of the j-th pipe. With the aim of increasing the accuracy, each finite element is split again into several sub-elements, say NSE. Then, by using the method of characteristics the species equations can be solved for this refined mesh [45]. More details can be found in Appendix A. It is worth mentioning that this method has less diffusion than other first order upwind methods [26].

In order to compute the gas velocity appearing in the transport equations at mesh-point x_m^j, the following formula is used (see Remark 4.1). Then, this velocity can be easily interpolated over the sub-elements of the finer mesh.

order to compute Φ_{n+1}^j [28,29]. Hence, the value of function $a(x, t)$ (see (8)) should be previously determined by using the mass fractions of species at time t_n which, indeed, have been already computed. This is the first stage of the n-th time step. In the second stage of the same time step, we compute mass fraction approximations at time t_{n+1} by using the gas velocity at time t_n interpolated along sub-elements. Thus, the flow and species equations are separately solved at each time step, leading to a *segregated* numerical method. As mentioned before, an interesting consequence is that different meshes for solving the flow and gas species equations are allowed which is an important feature of the overall method, improving its performance in terms of computing time versus accuracy. Fig. 3 shows a flowchart of the whole numerical method.

After computing the gas composition at time t_{n+1}, the gas properties are updated and the next time step begins. It should be noticed that two different forms of gas properties calculation have been implemented. In the first one, the gas properties along the pipes are calculated on each element and sub-element. In the second one, the average composition along each pipe is first calculated and then the gas properties corresponding to this average are used along the whole pipe. Numerical experiments show that the latter reduces the computational cost without significantly affecting the accuracy.

5. Numerical experiments

For computer implementation of the introduced numerical methods, a program in Fortran language has been written from scratch.

In order to validate this program and the overall methodology,

$$
u_{n,m}^j = \frac{1}{2\Delta t S^j} \frac{\Phi_{n+1}^j(x_m^j) - \Phi_{n-1}^j(x_m^j)}{\rho_{IC}(x_m^j) - 1 \Big/ S_j \left(\alpha (\Phi_{n+1}^j)_x(x_m^j) + \beta (\Phi_n^j)_x(x_m^j) + \gamma (\Phi_{n-1}^j)_x(x_m^j) \right) \Big/ (\alpha + \beta + \gamma)}, \quad n = 0, \ldots, M, \ m = 0, \ldots, NSE_j
$$

(42)

4.3. The overall numerical method

Notice that the flow equation and the gas species equations are coupled because, on the one hand, $a(x, t)$ defined in (8) depends on composition and, on the other hand, gas velocity $u(x, t)$ appears in the species transport equations (see Fig. 2). Let us recall that, for numerical solution, the flow equations are discretized at time t_n in

two test cases are addressed in this paper. The goal of the first one is to check the performance of the characteristics method implementation used to solve the species equations. In the second one, a small real network has been considered for which pressure, mass flow rate, and gas composition at the nodes have been experimentally measured.
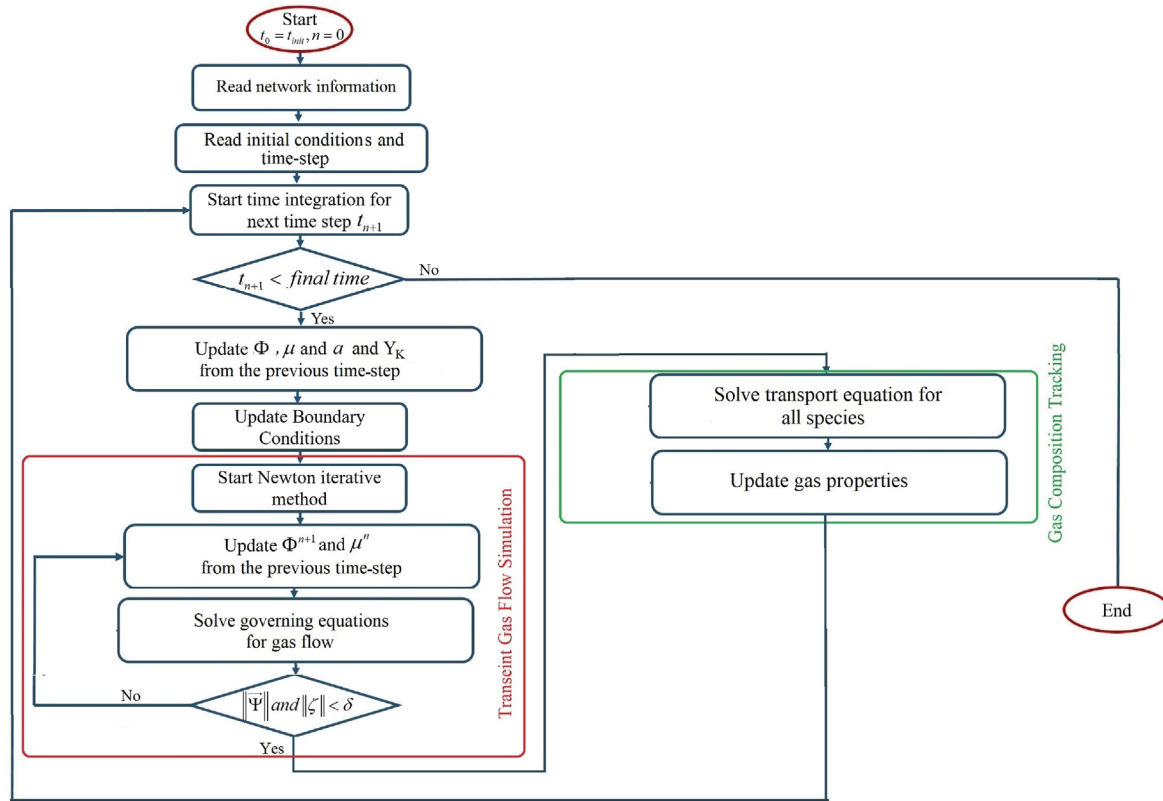
Fig. 3. Flowchart of the overall numerical method.

5.1. Case 1. solving advection equation

As it was mentioned in Section 3.2, in order to compute the gas composition along the network, equation (4) have to be solved for all pipes together with initial and boundary conditions. In this subsection, with the objective of evaluating the quality of the numerical solution of these equations, a problem with a given non-constant velocity along a pipe and discontinuous boundary conditions with respect to the initial condition is considered. After comparing the numerical results with the exact solution, the orders of accuracy in time and space have been calculated. For this purpose, the L^1-norm is used to compute the errors. More precisely, the error is computed as a discrete version of the double integral space and time,

$$\|e\|_1 = \int_0^T \int_0^L |W_{Numerical} - W_{Exact}| dxdt. \tag{43}$$

We consider the following initial-boundary value problem:

$$\frac{\partial W}{\partial t} + u(x,t)\frac{\partial W}{\partial x} = 0 \ \forall (x,t) \in [0,L] \times [0,T], \tag{44}$$

$$W(0,t) = W_R \ \forall t \in [0,T], \text{ if } u(0,t) > 0, \tag{45}$$

$$W(L,t) = W_L \ \forall t \in [0,T], \text{ if } u(L,t) < 0, \tag{46}$$

$$W(x,0) = W_{IC}(x) \ \forall x \in [0,L]. \tag{47}$$

The exact solution of (44)-(47) is

$$W(x,t) = W_{IC}(X(x,t)) \ \forall (x,t) \in [0,L] \times [0,T], \tag{48}$$

where $X(x,t)$ denotes the position at initial time of the *particle* that is located at point x at time t. It will be calculated following the characteristics lines (trajectories), as shown in Fig. 4.

In the simulation program for gas composition tracking, we have used a linear interpolation of the velocity along the sub-elements. Accordingly, in this test case, a given continuous linear velocity on each half of the pipe with respective positive and negative values has been considered (see Fig. 4). More precisely, $L = 1$ and

$$u(x,t) = \begin{cases} a_1 x + b_1 & \text{if } 0 < x < x^*, \\ a_2 x + b_2 & \text{if } x^* < x < 1, \end{cases}$$

with $x* = 0.5$.

We know that the equation of the characteristic line passing through point x_0 at initial time t_0 is $x = X(x_0, t)$, with $X(x_0, t)$ satisfying the initial-value problem
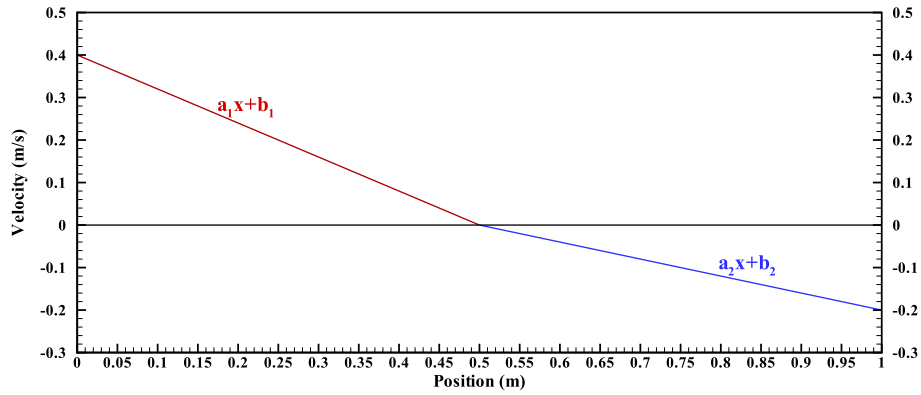
Fig. 4. Velocity along the pipe.

$$\frac{dX(x_0, t)}{dt} = u(X(x_0, t), t), \tag{49}$$

$$X(x_0, t_0) = x_0. \tag{50}$$

The exact solution of this problem can be easily obtained:
If $0 < x < x^*$, then

$$\int_{x_0}^{x} \frac{dx}{a_1 x + b_1} = \int_{t_0}^{t} dt, \tag{51}$$

and hence

$$X(x_0, t) = \frac{a_1 x_0 + b_1}{a_1 e^{a_1 t}} - \frac{b_1}{a_1}. \tag{52}$$

In a similar way if $x^* < x < 1$, then

$$\int_{x_0}^{x} \frac{dx}{a_2 x + b_2} = \int_{t_0}^{t} dt, \tag{53}$$

and hence

$$X(x_0, t) = \frac{a_2 x_0 + b_2}{a_2 e^{a_2 t}} - \frac{b_2}{a_2}. \tag{54}$$

Therefore, the exact solution W is given by

$$W(x, t) = \begin{cases} W_L & \text{if} & 0 < x < \frac{b_1}{a_1}(e^{a_1 t} - 1), \\ W_{IC} & \text{if} & \frac{b_1}{a_1}(e^{a_1 t} - 1) \le x \le 1 - \frac{b_2}{a_2}(e^{a_2 t} - 1), \\ W_R & \text{if} & 1 - \frac{b_2}{a_2}(e^{a_2 t} - 1) < x < 1, \end{cases} \tag{55}$$

and hence has two jump discontinuities in the spatial variable x, at any time.

Now, let us take $a_1 = -0.8$, $b_1 = 0.4$, $a_2 = -0.4$, $b_2 = 0.2$ (see Fig. 4), and initial and boundary conditions given by $W_{IC} = 0.50$, $W_L = 1.0$ and $W_R = 0.0$. The numerical results for $\Delta t = 0.02$ s, 200 meshes and sub-mesh refinements corresponding to $NSE_n = 2^n$, $n = 0, 1, 2, 3$ are presented in Fig. 5.

Function $W(., t)$ is plotted versus the longitudinal position in the pipe at several time instants: $t = 1, 2, 3$, and 4 s. It should be noticed that, since the velocity is positive (respectively, negative) on the left half (respectively, on the right half) of the pipe, boundary conditions need to be given at the two ends, which propagate towards the center of the pipe. It is also clear that the propagation of W over time is different in the two pipe halves because the velocity is not *symmetric* in size about the midpoint $x^* = 0.5$.

The L^1-norm of the error corresponding to different meshes and times are presented in Tables 1 and 3. Besides, Tables 2 and 4 show the orders of accuracy in time and space, respectively. To calculate the order of accuracy in space, the L^1-norm of the error for several meshes has been computed by considering a small time step. Similarly, for the order of accuracy in time, a small spatial mesh-size is taken and then the L^1-norm is computed for several time steps. As expected, these tables show that both orders of accuracy for time and space discretizations are close to 1.

5.2. Case 2. a real transportation network

The second test concerns a small real network included in the Spanish gas transportation network. For this network, pressure, energy flow rate and mass fractions of gas species are measured experimentally at some nodes. The network contains 11 nodes: nodes 2 and 7 are structural nodes (exchanged mass flow rate with the outside is null) so there are not measurements for them.

The schematic topology of the network is given in Fig. 6 and the height along the pipes, $h(x)$, can be seen in Figs. 7−9. Table 5 shows the topological and geometrical data of the network. Input data for numerical simulation as well as the list of species in the gas mixture are given in Tables 6 and 7, respectively.

Measurements of pressure and energy flow rates at nodes are known for 19 days. Additionally, the gas composition at nodes 1, 5, and 10 are also available. For validation purposes, the input/output mass flow rates, $c^i(t)$, are given at all nodes except at node 1 where pressure is prescribed. Next, the mass flow rate at node 1 and pressure at the rest of the nodes are computed with our method
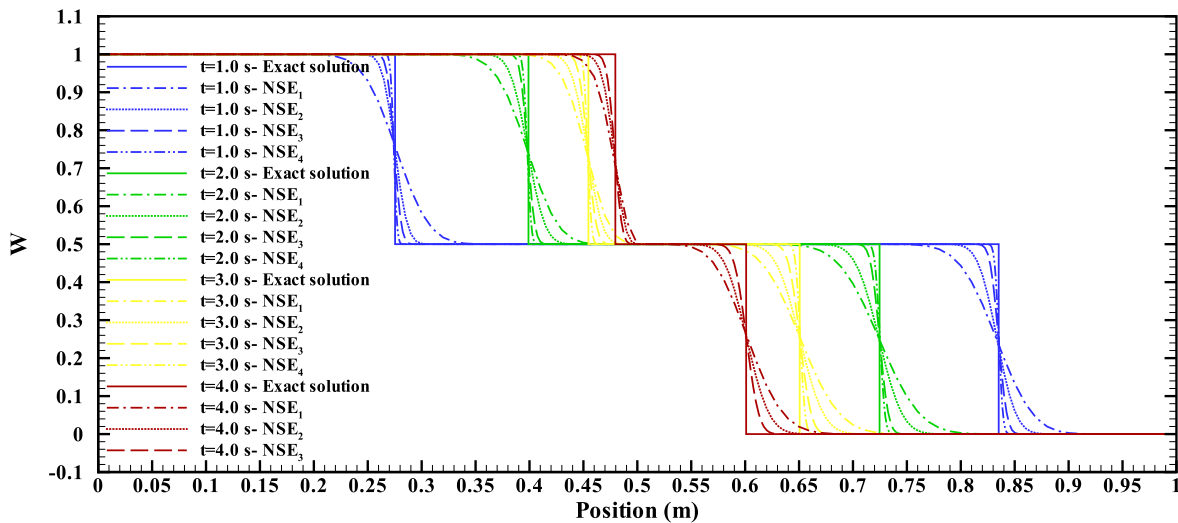
Fig. 5. Numerical results for different sub-meshes and times.

Table 1
L^1-norm for Mesh = 500 and different sub-meshes, and $\Delta t = 10^{-2}$.

	$NSE_1 = 1$	$NSE_2 = 2$	$NSE_3 = 4$
L^1-norm	0.02223	0.01081	0.00544

Table 2
Order of accuracy in space and $\Delta t = 10^{-2}$.

	$\log(E_{NSE_1}/E_{NSE_2})/\log(2)$	$\log(E_{NSE_2}/E_{NSE_3})/\log(2)$
W	1.04	0.99

Table 3
L^1-norm for different time step and Mesh = 1000, sub-mesh = 8.

	$\Delta t_1 = 0.500$	$\Delta t_2 = 0.250$	$\Delta t_3 = 0.125$
L^1-norm	0.0726	0.0383	0.0195

Table 4
Order of accuracy in space for Mesh = 1000, and sub-mesh = 8.

	$log(E_{\Delta t_1}/E_{\Delta t_2})/\log(2)$	$log(E_{\Delta t_2}/E_{\Delta t_3})/\log(2)$
W	0.922	0.973

and then compared with their respective measurements over time. Moreover, the mass fraction of species along the time are given at node 1, as it is the input node. After calculations, a comparison between the numerical and the measured mass fractions at consumption nodes 5 and 10 are shown.

The prescribed pressure at node 1 over time is shown in Fig. 10, while the flow rates in GWh/d that are imposed at all other nodes can be seen in Figs. 11 and 12.

It should be mentioned that, in the general implementation, the nodal boundary condition for the mass fractions of species is instantaneously switched on or off according to the sign of the flow rate at the node as follows: if the energy flow rate is zero or negative, the gas composition does not affect the solution because the gas does not enter the network through this node. Hence, it is switched off. The mass fractions of the three dominant gas species at node 1 are plotted in Figs. 13–15.

Before showing the numerical results, let us make some general remarks about this test:

1. The flow rate at nodes are given in GWh/d (energy flow rate) but the data of the governing flow equation are mass flow rates in kg/s. Hence, according to the calculated nodal gas composition at each time step, the conversion factor is calculated and then the energy flow rate is converted to kg/s.
2. As mentioned above, the flow equation and the gas species equations are solved separately. This gives us the possibility to consider different meshes for flow and species equations which leads to have more accurate results from the gas species equation without increasing the overall computational cost, as a rather coarse mesh for solving the flow equation can be used.
3. The results corresponding to the two forms of computing the gas properties at each time step, described above, are identified by **-Var** and **-Avr.** Recall that they refer, respectively, to variable gas properties and average gas properties along the pipes.
4. The code has run in a system with an Intel(R) Core(TM) i7-8565U @ 1.8 GHz processor with 16.00 Gb RAM and 8 Mb cache but only one core has been used. The real run-time for the simulation of 19 days (456 h) is around 75 s. The real run-times for different choices of the number of sub-elements are given in Table 8. From this table, one can deduce that the dominant run time is mainly devoted to solve the flow equation. In fact, increasing the number of sub-element improves the accuracy but the computational time does not increase significantly. This interesting feature confirms the ability of the present method to simulate real-time operations in gas transportation networks with high accuracy and low computational cost.
5. Regarding error analysis of this second test case, let us introduce the relative L^1-like norm by
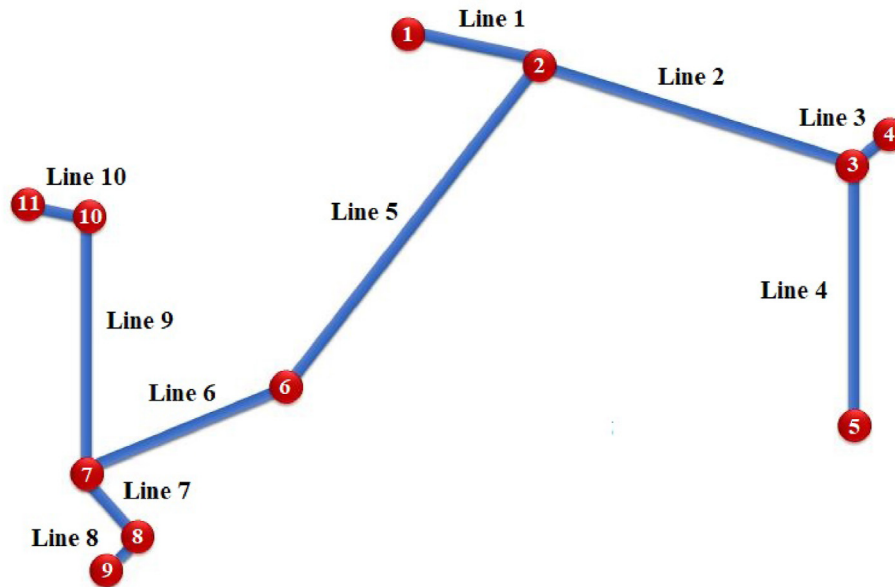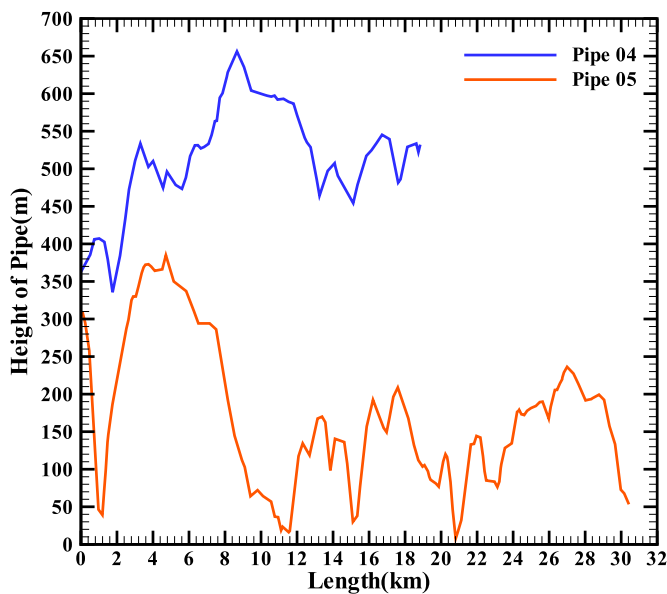
Fig. 6. Topology of the real network.

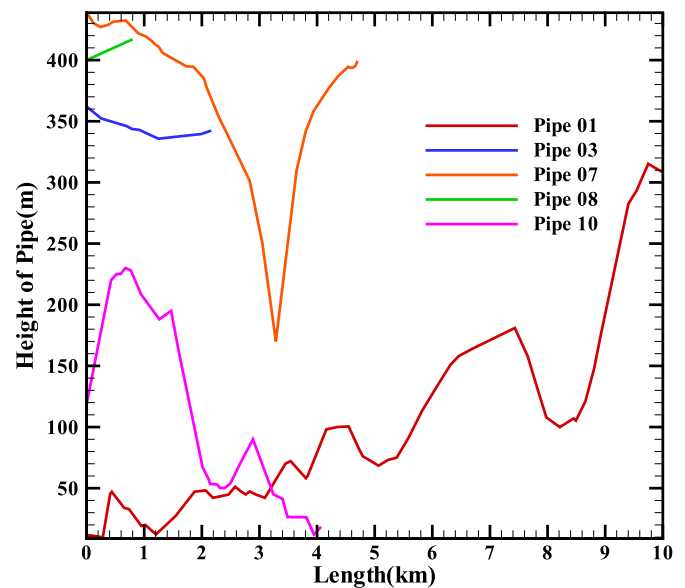**Fig. 7.** Height of pipes #4, #5, and #6.

Fig. 8. Height of pipes #1, #3, #7, #8, and #10.

$$\|e\|_{1,rel} = \int_0^T \left| \frac{\mathcal{N}_{Numerical} - \mathcal{N}_{Experimental}}{\mathcal{N}_{Experimental}} \right| dt. \tag{56}$$

Then, the average relative error is defined as a discrete version of (56). More precisely,

$$\|e_N\|_{1,rel} = \frac{1}{M} \sum_0^{M-1} \left| \frac{\mathcal{N}_{Numerical} - \mathcal{N}_{Experimental}}{\mathcal{N}_{Experimental}} \right|. \tag{57}$$

Now, numerical results are shown and analyzed. Figs. 16–20

show the variation of pressure along the time at nodes 4, 6, 8, 9, and 10, respectively. These nodes are selected from different parts of the network and have zero or negative consumption (either structural or output nodes). One can see that, in general, the numerical results obtained with the presented method are in good agreement with the experimental data. There is some discrepancy between the numerical results and the experimental data over some small time intervals but, based on the good agreement in other intervals, it is likely due to errors in measurement devices and procedures. It should be mentioned that, in particular, the energy flow rate at node 1 is not very accurate but it is worth mentioning that the energy flow rate is not directly measured. In fact, it is
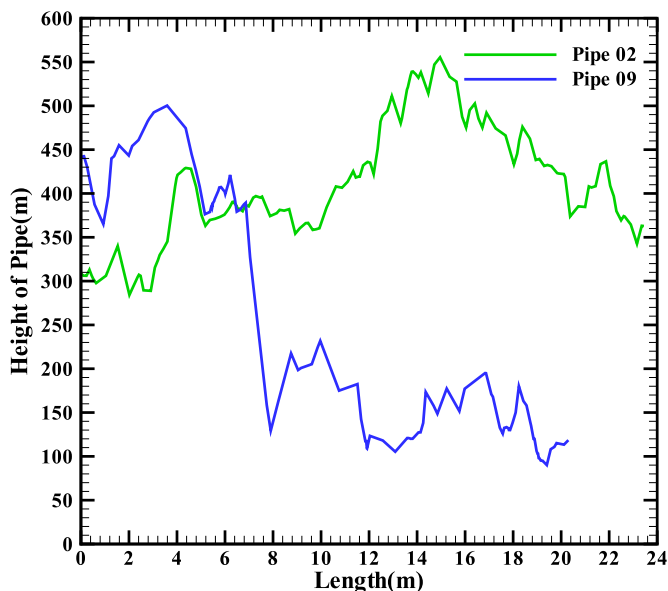
Fig. 9. Height of pipes #2 and #9.

fractions, several numbers of sub-elements to create the mesh and solve the species equations have been used. A comparison of the numerical results with the experimental data for different number of sub-elements can be seen in Fig. 27. The conclusion is that as the number of sub-elements increases, the gas composition is computed more accurately. More precisely, taking the number of sub-elements equal to 20, the computed gas composition is in good agreement with the experimental data. Also, unlike many numerical methods, our method can easily capture the sharp variation in the gas composition.

Notice that, as shown in Figs. 21—26, the tracked gas composition by the present numerical method is congruent with the measured data. In Figs. 21—23 and Figs. 24—26, the variation of the three dominant species at nodes 5 and 10, is shown. The small differences are likely due to errors in gas species measurements at the input and/or output nodes. In particular, the discrepancy between numerical results and measurements observed in Fig. 23 seems to be caused by errors in species measurements. In general, the gas composition at the consumption nodes is not only a function of the gas composition at the input nodes, but also depends on the existing stored gas in the network. The delivery of the gas from emission nodes to consumption nodes will be influenced

Table 5
Pipe data for the real network.

Pipe	Inlet Node	Outlet Node	Diameter (in)	Length (km)	Roughness (mm)
1	1	2	30	9.99	0.010
2	2	3	26	23.448	0.00001
3	3	4	16	2.163	0.010
4	4	5	20	18.842	0.010
5	5	6	26	30.431	0.010
6	6	7	16	15.680	0.00001
7	7	8	10	4.702	0.00001
8	8	9	10	0.8	0.010
9	7	10	16	20.300	0.010
10	10	11	16	4.070	0.010

Table 6
Data for the second test.

Parameter	Notation	Value	Unit
Temperature	θ	11.0	^{0}C
Simulation time	T	456	h (hour)
Time step	Δt	30	s (second)
Element size	Δx	4000	m (meter)

Table 7
Species in the gas mixture.

Components	CH_4	C_2H_4	C_3H_8	C_4H_{10}	C_5H_{12}	N_2	CO_2

computed from other variables which include the mass fractions of species. Another point that can be deduced from the figures is that increasing the number of sub-elements to solve the species equations does not lead to significant changes in the computed nodal pressures.

The mass fractions of the three dominant gas species at nodes 5 and 10 are shown in Figs. 21—26. In order to track these mass

by the distance and the velocity of the gas within the pipes over time. In the present case, the gas is only introduced at node 1 and therefore the gas at the consumption nodes should have the same composition as the gas at the emission node with some delay. This delay is related to the gas velocity and also to the existing gas inside the network at initial time. However, as it can be seen in Fig. 23, the measured mass fraction of C_3H_8 at node 5 is not in the same range as the measured mass fraction of C_3H_8 in the gas introduced at node 1 (see Fig. 15). As illustrated in Fig. 28, in contrast to measurements, the numerical results are quite reasonable and coherent. Fig. 29 shows the comparison between the measured mass fraction of C_3H_8 in the gas delivered at node 10, and the numerical results. Unlike node 5, the measurements and numerical results at node 10 agree well and also with the mass fraction of C_3H_8 at node 1. Finally, Fig. 30 shows mass conservation of the first three dominant species at nodes 2, 3, and 7. It can be seen that, as expected, species are conserved at nodes up to computer precision. It is important to highlight that, unlike the flow equation, an explicit method is used to solve the species equations. Therefore, we cannot consider a very large time step for the whole numerical method. On the other hand, in the present computations the characteristic curves are linearly approximated so the scheme is only first order accurate. However, it
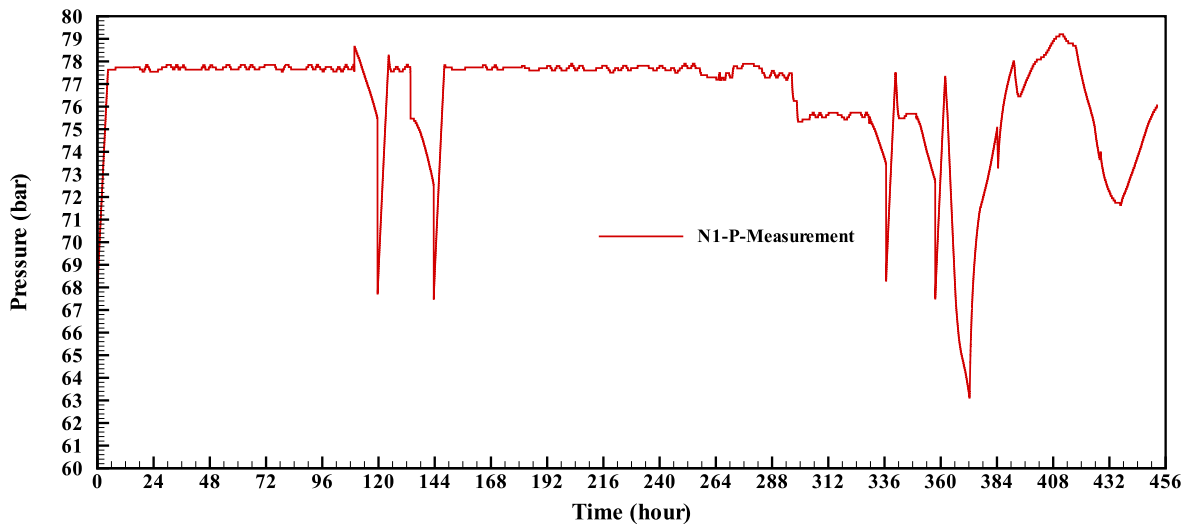
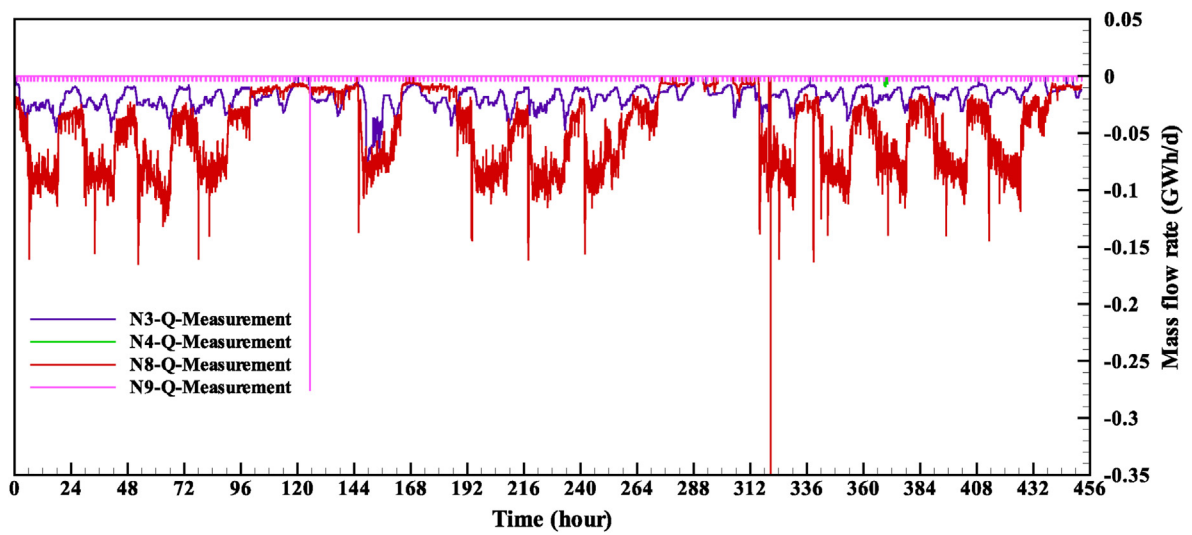**Fig. 10.** Boundary condition: measured pressure at node 1.

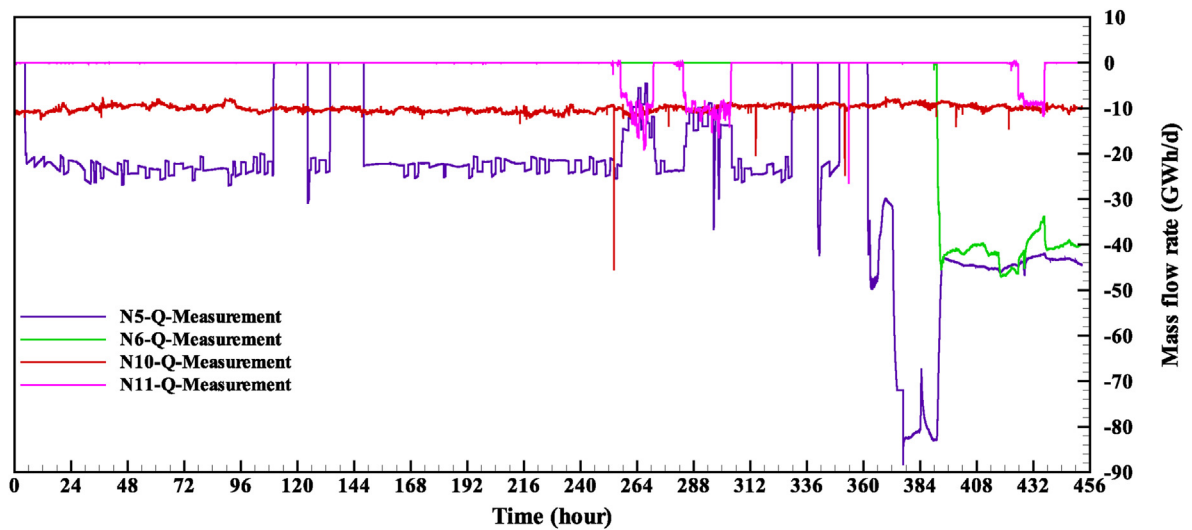**Fig. 11.** Boundary condition: measured energy flow rate at nodes 3,4, 8, and 9.

Fig. 12. Boundary condition: measured energy flow rate at nodes 5, 6, 10, and 11.
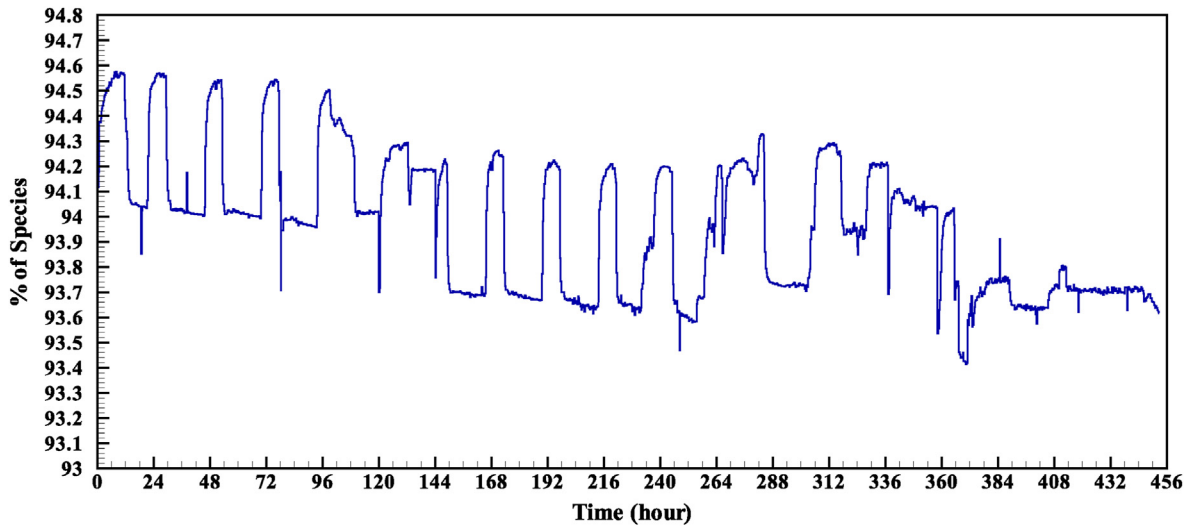
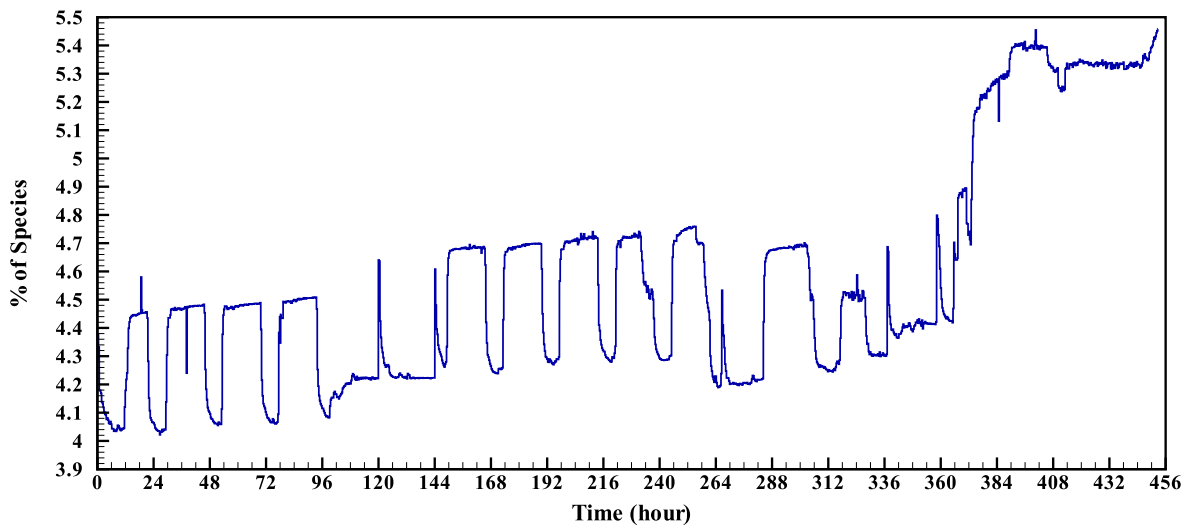**Fig. 13.** Boundary condition: measured %CH4 at node 1.

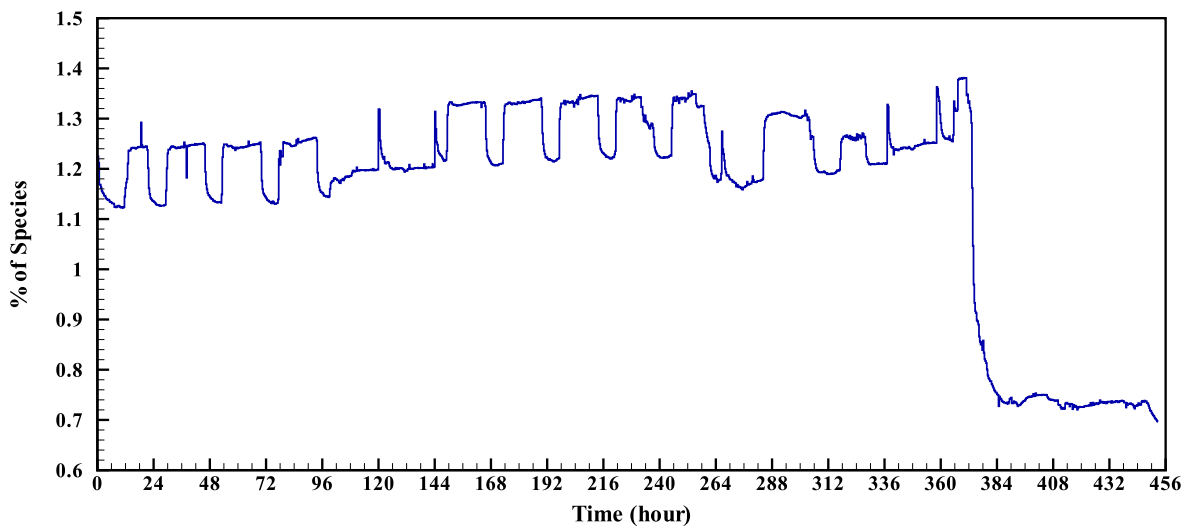**Fig. 14.** Boundary condition: measured %C2H6 at node 1.

Fig. 15. Boundary condition: measured %C3H8 at node 1.

Table 8
Real run time for the experimental case.

Experiment time: 19 days	$\Delta t = 30$ s	Run time (seconds)
Number of sub elements	$\Delta x = 4000$ m	
1		$\simeq 69$
10		$\simeq 74.5$
20		$\simeq 76$
40		$\simeq 77$

are presented. As shown in Table 9, the average relative error of the pressure for all selected nodes is between 0.45 and 0.85% (%). Even more, maybe the average relative error is below these values because in some intervals the pressure measurements seem not to be quite accurate. Moreover, Table 10 shows that the average relative error of the three dominant species at nodes 5 and 10 is between 0.15 and 1.5% (%) depending on the number of sub-elements (NSE). As mentioned above, it can be seen that more ac-
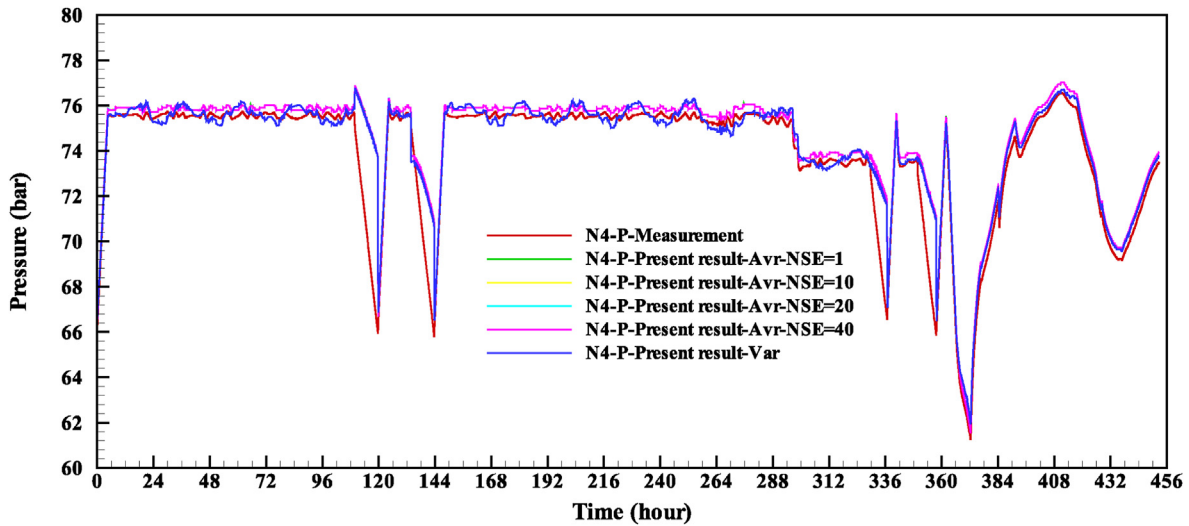
Fig. 16. Comparison of numerical results with measurements: pressure at node 4.
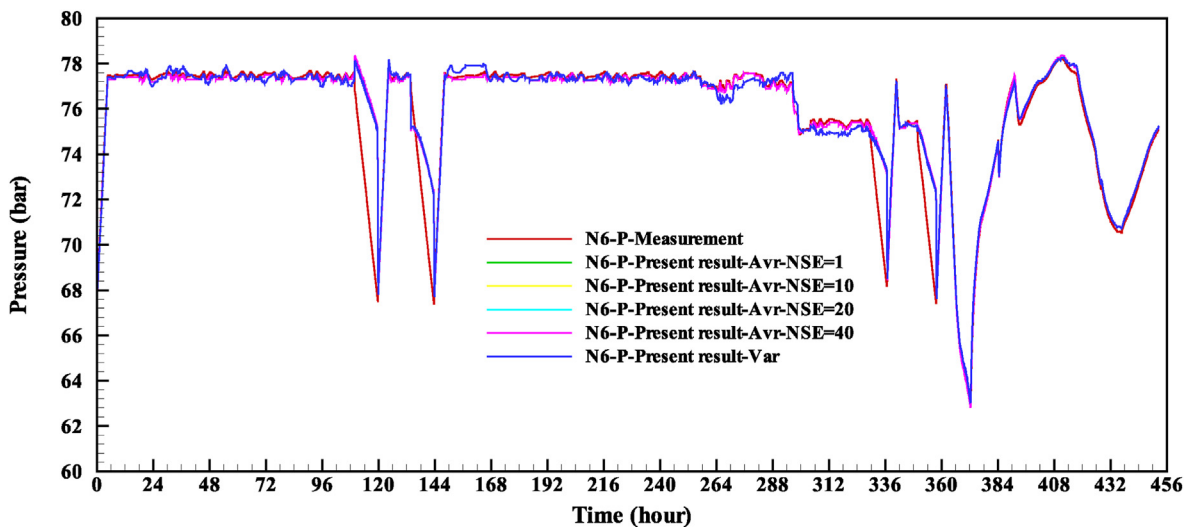
Fig. 17. Comparison of numerical results with measurements: pressure at node 6.

should be noticed that, by considering second-order interpolation this could be improved. Moreover, compared to many numerical methods, the method of characteristics has the ability to capture the sharp variation in the gas composition without spurious oscillations.

Finally, in Tables 9 and 10, the average relative error with respect to the experimental data of pressure and mass fractions of species

curate results are obtained for gas composition by increasing the number of sub-elements. On the other hand, the average relative error for C_3H_8 at node 5 is around 8%. As discussed for Figs. 23 and 28, and compared to other tracked species, the measurement seems to include some errors. This fact could explain why the average relative error is considerably higher than for other species.
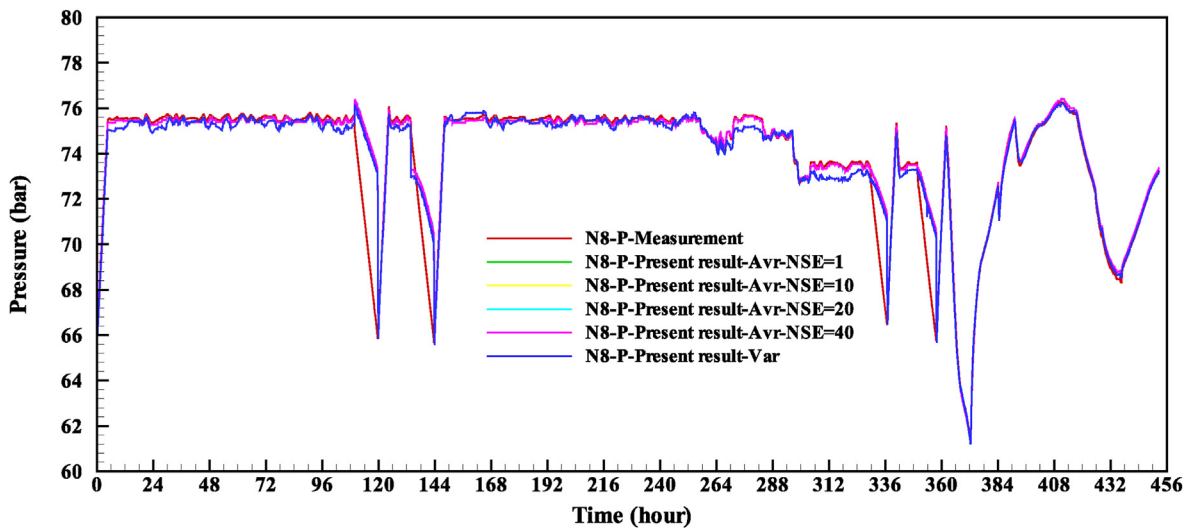
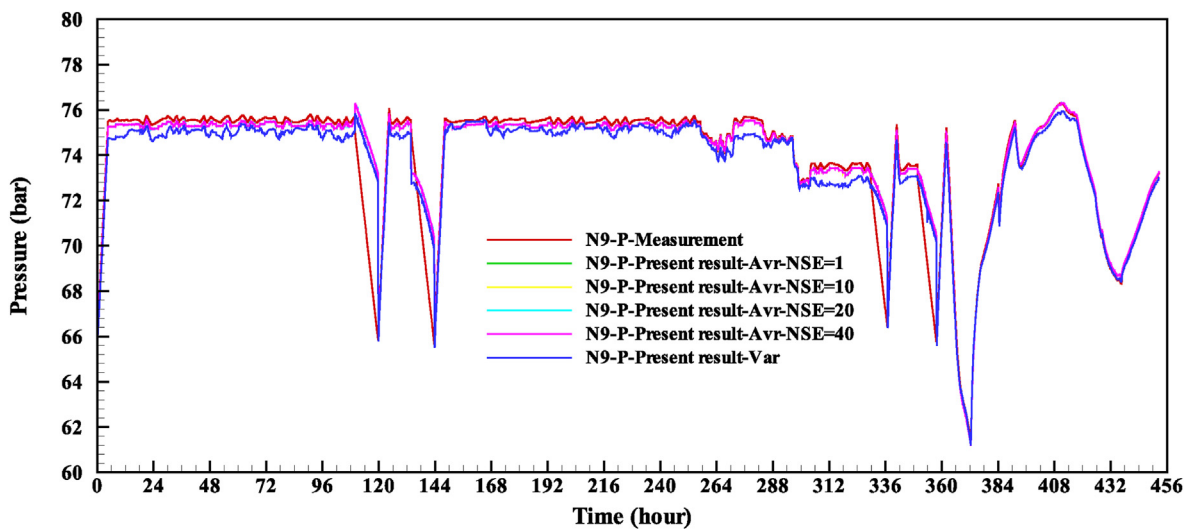**Fig. 18.** Comparison of numerical results with measurements: pressure at node 8.

Fig. 19. Comparison of numerical results with measurement of pressure at node 9.
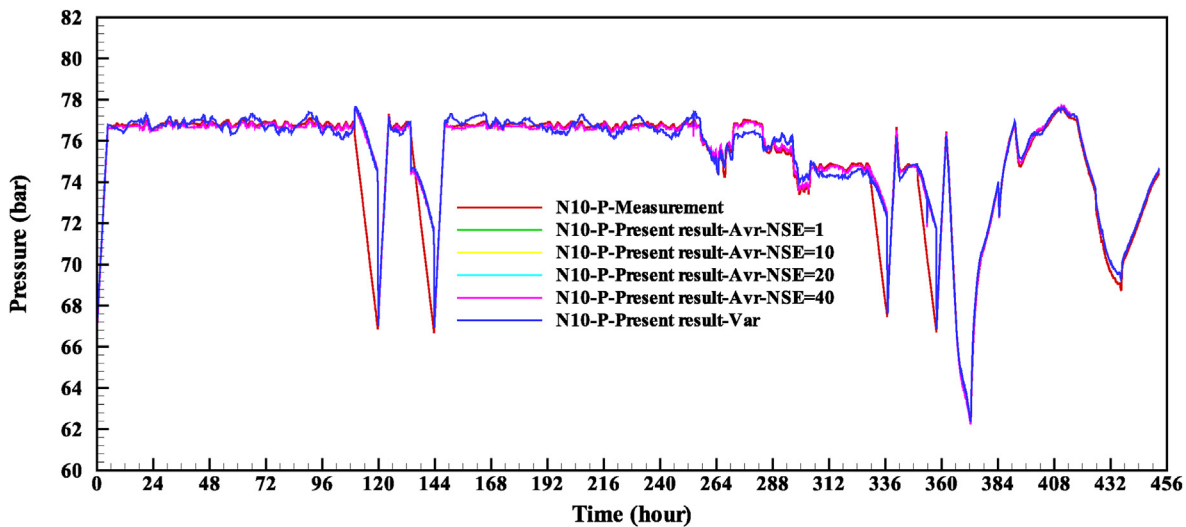

Fig. 20. Comparison of numerical results with measurements: pressure at node 10.
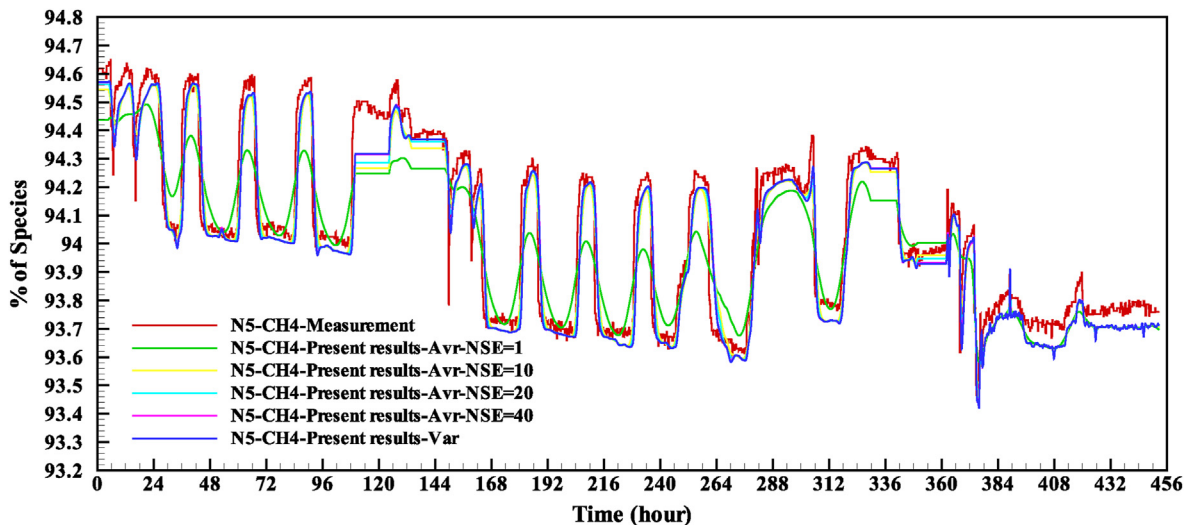
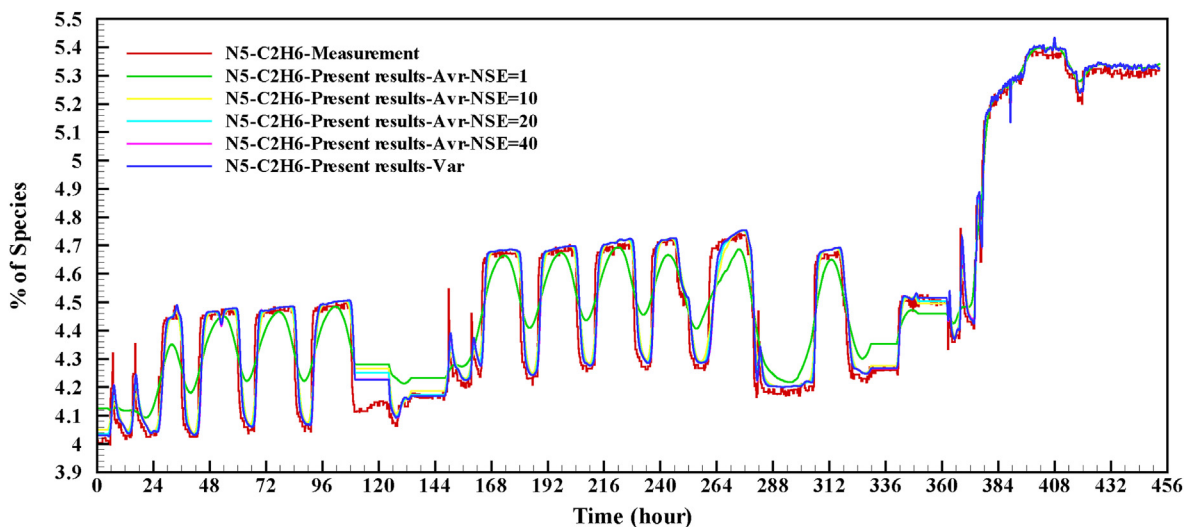**Fig. 21.** Comparison of numerical results with measurement of %CH4 at node 5.

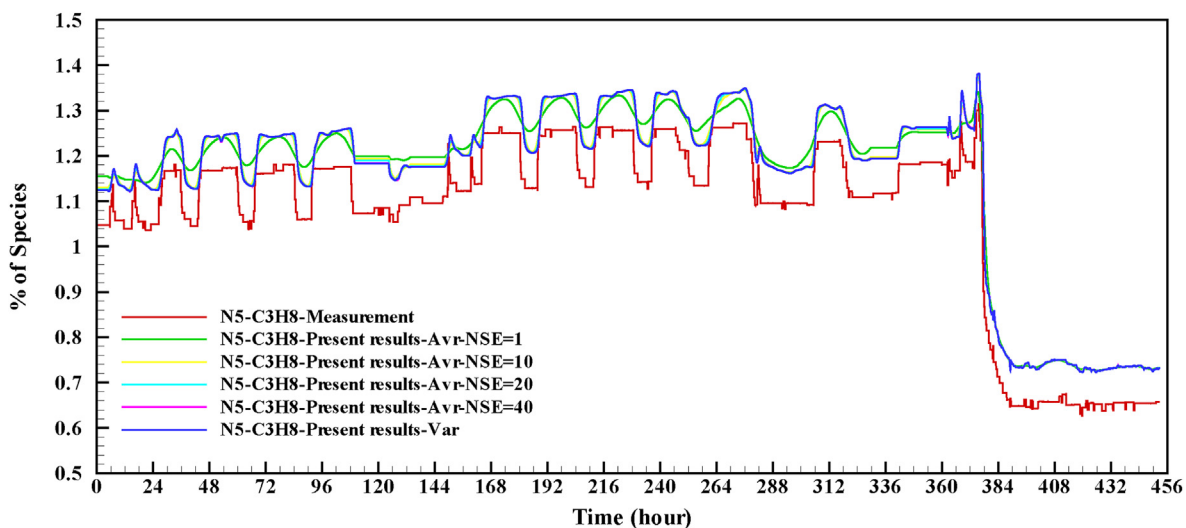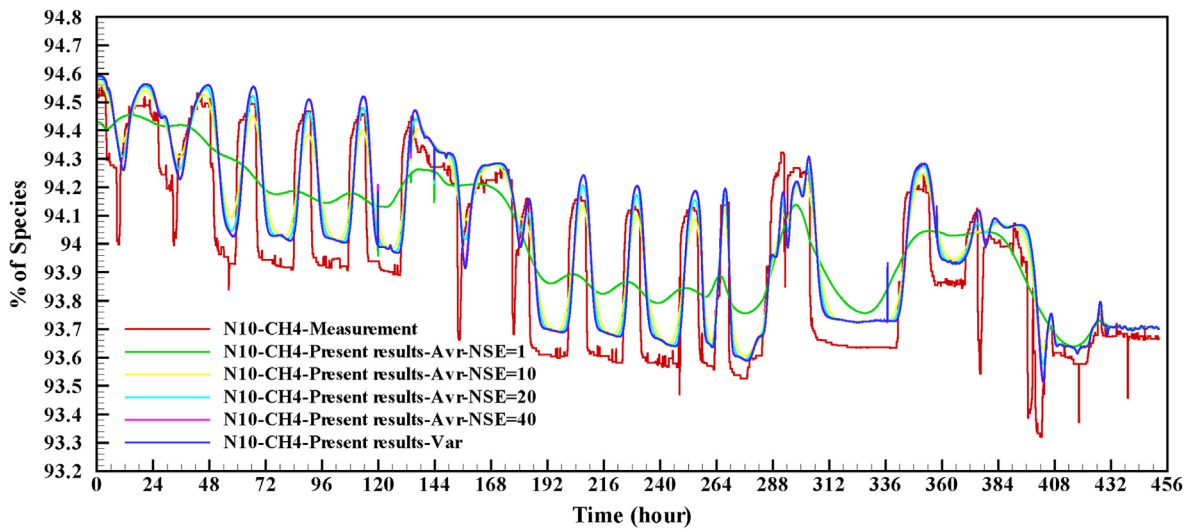**Fig. 22.** Comparison of numerical results with measurements: %C2H6 at node 5.

Fig. 23. Comparison of numerical results with measurements: %C3H8 at node 5.

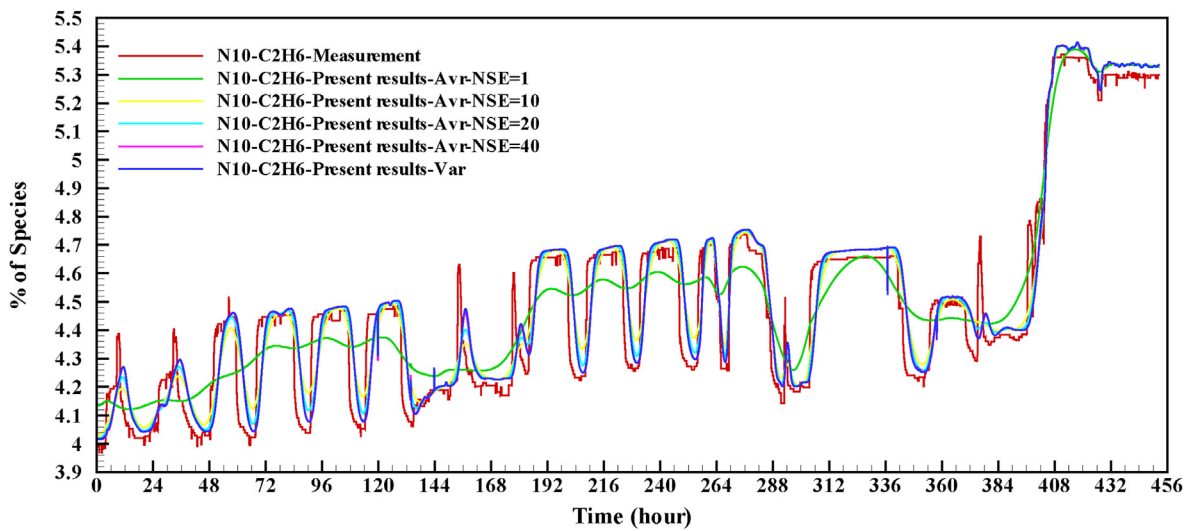**Fig. 24.** Comparison of numerical results with measurements: %CH4 at node 10.

Fig. 25. Comparison of numerical results with measurements: %C2H6 at node 10.
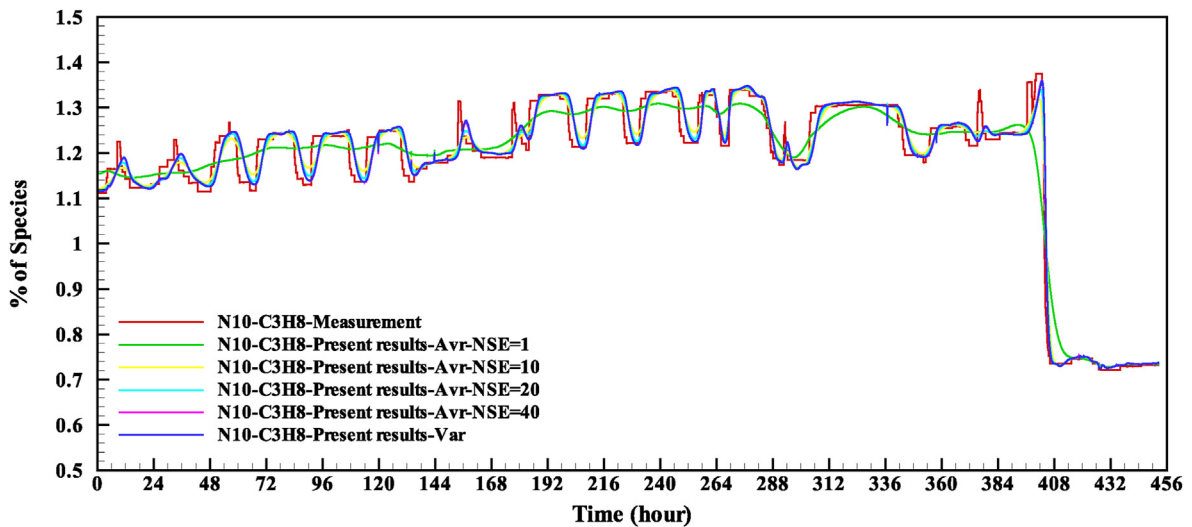

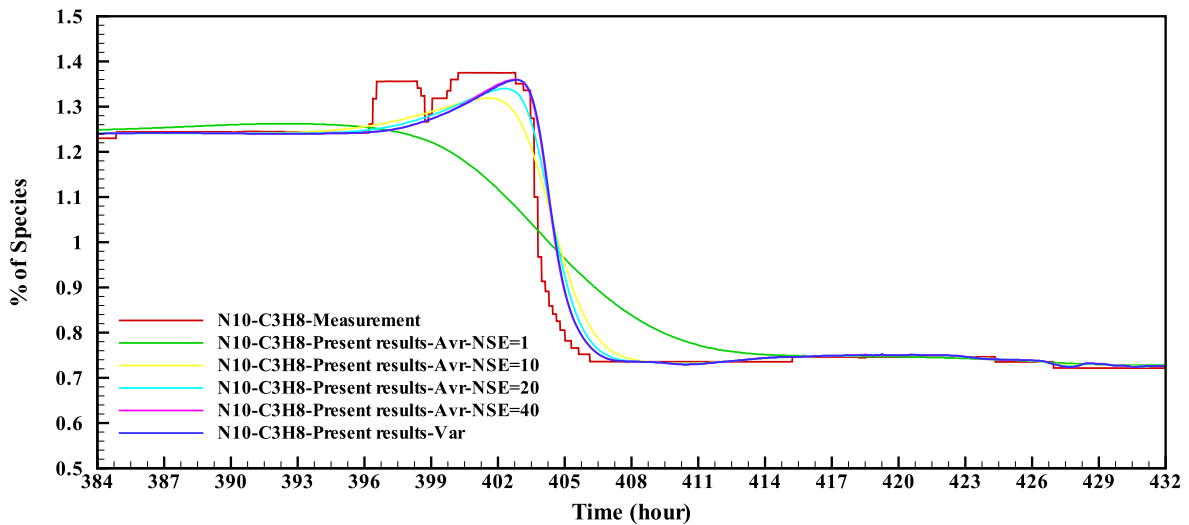**Fig. 26.** Comparison of numerical results with measurements: %C3H8 at node 10.

Fig. 27. Comparison of numerical results with measurement: %C3H8 between hours 384 and 432.
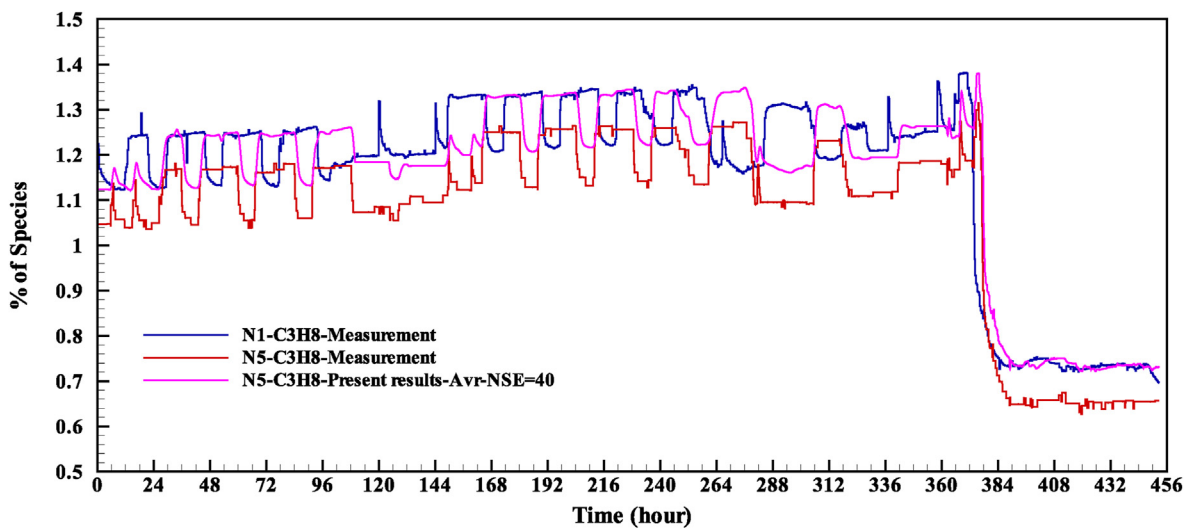

Fig. 28. Comparison of numerical results with measurements: %C3H8 at nodes 1 and 5.
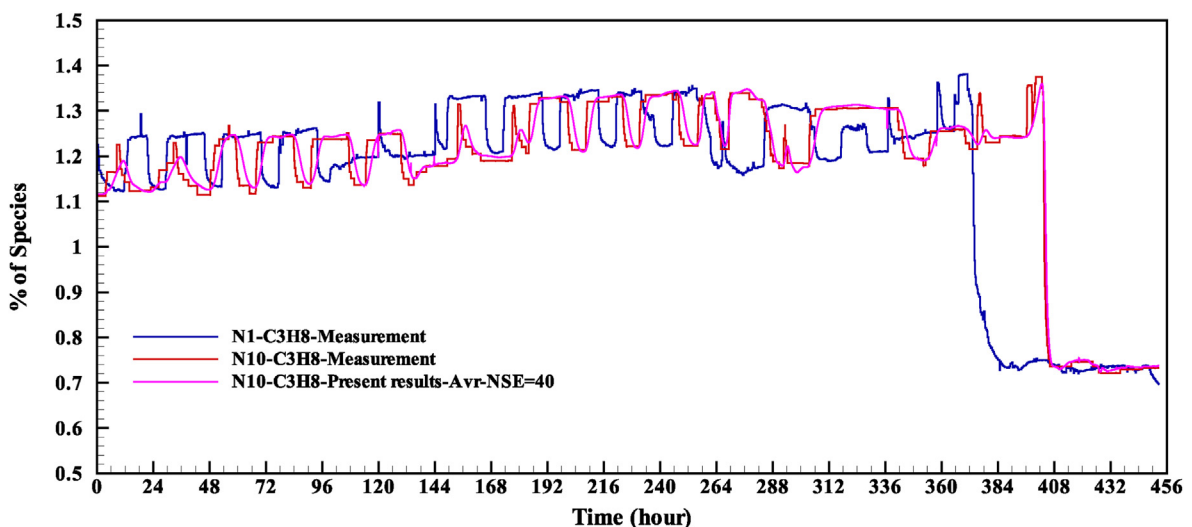

Fig. 29. Comparison of numerical results with measurements: %C3H8 at nodes 1 and 10.
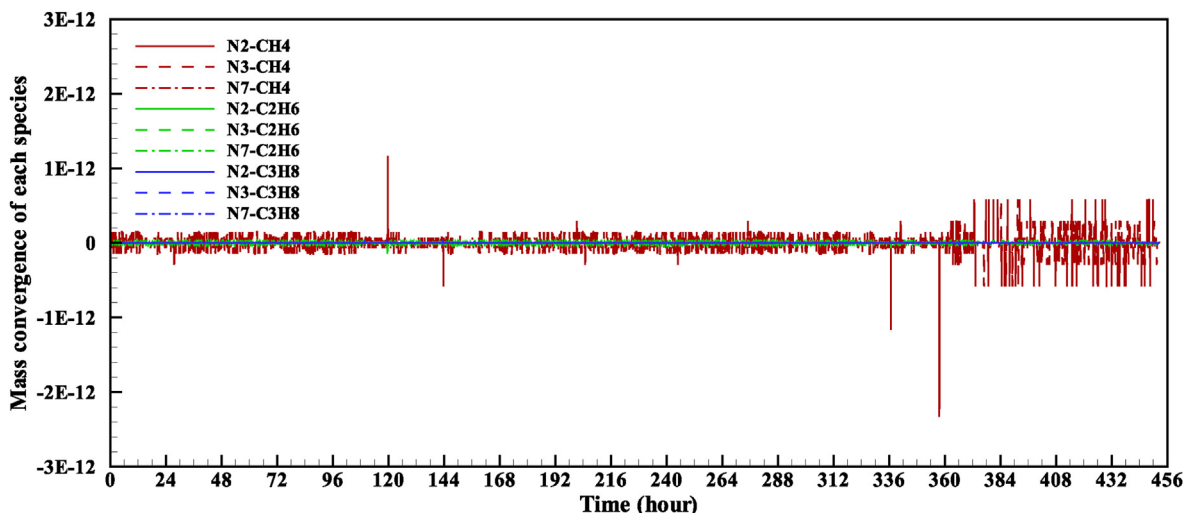
Fig. 30. Mass conservation of the dominant species at some selective nodes.

Table 9
Relative error of the computed pressure with respect to experimental data (%).

NSE	Node 4	Node 6	Node 8	Node 9	Node 10
Avr-1	0.8432	0.4801	0.4781	0.5491	0.4925
Avr-10	0.8430	0.4801	0.4785	0.5494	0.4922
Avr-20	0.8431	0.4801	0.4785	0.5494	0.4922
Avr-40	0.8429	0.4801	0.4786	0.5495	0.4921
Var-40	0.7305	0.5667	0.5840	0.8178	0.6511

Table 10
Relative error of the mass fractions of species with respect to experimental data (%).

NSE	Node 5			Node 10		
	CH_4	C_2H_6	C_3H_8	CH_4	C_2H_6	C_3H_8
Avr-1	0.1149	1.7831	8.1728	0.1746	2.5269	2.7890
Avr-10	0.0742	0.9446	7.9344	0.1212	1.6435	1.6230
Avr-20	0.0706	0.8573	7.9006	0.1182	1.5795	1.5387
Avr-40	0.0697	0.8281	7.8854	0.1206	1.5903	1.5455
Var-40	0.0695	0.8215	7.8906	0.1201	1.5875	1.5452

6. Conclusions

In this research, a method has been introduced to track gas composition in a transportation network. It is a natural complement to a method proposed in previous articles by the authors to simulate the flow of a gas mixture with a given constant composition. Unlike most of the references on the subject, a segregated method has been developed that solves the flow and species equations separately. Thanks to the weak coupling, two different numerical methods can be used, as well as two different meshes. More precisely, a second-order finite element method was chosen for the flow equation on a coarse mesh and a first-order characteristic method for the species equation on a finer mesh. This is an interesting feature of the method because accurate results can be obtained for monitoring gas composition without increasing the overall computational cost. Another important property of the proposed method is that it conserves exactly the mass of species. It is also worth mentioning that the method of characteristics that has been used to solve the species transport equations has less diffusion than other first-order windward methods. In order to evaluate the performance of the method, two test cases have been addressed.

The first case is used to check the quality of the numerical solution of the species transport equation, and the second refers to a small real network in which the pressure, the energy flow and the composition of the mixture have been experimentally measured. From the second test case it can be deduced that the numerical results agree well with measurements and even reveal certain possible inconsistencies in the measurements.

Two drawbacks of our study could be raised. First, unlike the flow equation, we have used an explicit first-order characteristic method to solve the species equations. In this way, the characteristic line passing through each point is approximated linearly so we cannot take a very large time step for the whole numerical method. It should be noted that, by considering second-order interpolated points, we could improve this feature.

Second, a limitation of our study is that temperature must be given, since the energy equation is not included in the model. But, in general, this is not a practical problem because most gas transportation networks are underground and therefore the temperature can be accurately estimated. In any case, the inclusion of the energy equation in the model and the subsequent numerical solution can be done with a similar methodology to the equations for mass fractions of species; it will be the subject of a forthcoming study.

We conclude that the proposed method allows simulating real gas transportation networks with enough accuracy and low computational cost, which opens the door to consider practical control and dynamic optimization problems. It should be mentioned that within the framework of the energy transition, one of the recent interests is injection and transport of hydrogen, bio-methane or bio-gas in natural gas networks. In this context, numerical simulation of real networks with several gas inputs of different qualities is an important issue that can be addressed with the methodology presented in this article.

Credit author statement

Alfredo Bermudez: Conceptualization, Methodology, Writing. **Mohsen Shabani**: Methodology, Software, Validation, Data Curation, Writing.

Declaration of competing interest

The authors declare that they have no known competing

financial interests or personal relationships that could have appeared to influence the work reported in this paper.

Acknowledgment

Appendix A. Numerical Solution of the Transport Equation: Method of Characteristics

In this appendix, we describe a method of characteristics to solve the transport equations (see, for instance Ref. [45]). Let us consider the initial-boundary value problem for the transport equation

$$\frac{\partial Y}{\partial t}(x,t) + u(x,t)\frac{\partial Y}{\partial x}(x,t) = f(x,t) \text{ in } (0,L)\times[0,T], \quad (A.1)$$

$$Y(0,t) = Y_{left}(t) \text{ if } u(0,t) > 0, \quad (A.2)$$

$$Y(L,t) = Y_{right}(t) \text{ if } u(L,t) < 0, \quad (A.3)$$

$$Y(x,0) = Y_0(x) \text{ in } (0,L). \quad (A.4)$$

The main remark is that the sum of the left-hand terms of (A.1) is the material (or total) derivative with respect to time of Y, to be denoted $\frac{DY}{Dt}(x,t)$. Indeed, let us consider the motion with velocity u. More precisely, let us denote by $\tau \to X(x,\tau)$ the trajectory of this motion starting at point x at time t. In other words, $X(x,\tau)$ is the position at time τ of the material point that occupies position x at time t. For each x, $t \to X(x,\tau)$ is the solution of the initial-value problem

$$\frac{dX}{d\tau}(x,\tau) = u(X(x,\tau),\tau), \quad (A.5)$$

$$X(x,t) = x, \quad (A.6)$$

and we have,

$$\frac{DY}{D\tau}(x,\tau) = \frac{dY}{d\tau}(X(x,\tau),\tau) = \frac{\partial Y}{\partial \tau}(x,\tau) + u(x,\tau)\frac{\partial Y}{\partial x}(x,\tau).$$

Therefore, (A.1) can be rewritten as

$$\frac{dY}{d\tau}(X(x,\tau),\tau) = f(X(\tau;(x,\tau)),\tau)$$

This equality means that along the trajectory through point (x,t),

$$Y(X(x,\tau_2),\tau_2) = Y(X(x,\tau_1),\tau_1)$$
$$+ \int_{\tau_1}^{\tau_2} f(X(x,s),s)\,ds \quad \forall\ \tau_1 < \tau_2.$$

and by taking $\tau_2 = t$,

$$Y(x,t) = Y(X(x,\tau_1),t_1) + \int_{\tau_1}^{t} f(X(x,s),s)\,ds.$$

Now, choosing $t = t_{n+1}$ and $\tau_1 = t_n$ we get

$$Y(x,t_{n+1}) = Y(X(x,t_n),t_n) + \int_{t_n}^{t_{n+1}} f(X(x,s),s)\,ds$$

Therefore, if $X(x,s)$ for $s \in [t_n, t_{n+1}]$, and the integral on the right-hand side could be exactly computed, then $Y(x,t_{n+1})$ would also be exactly computed from the previous formula. However, in general one cannot solve the equation of trajectories exactly so, in practice, $Y(x,t_{n+1})$ has to be approximated by a function $Y_{n+1}(x)$. For instance,

$$Y^{n+1}(x) = Y^n(X_{\Delta t}(x,t_n)) + \Delta t\frac{f(x,t_{n+1}) + f(X_{\Delta t}(x,t_n),t_n)}{2},$$

where $X_{\Delta t}((x,t_n))$ is an approximation of $X((x,t_n))$ given, for example, by the explicit Euler scheme:

$$X_{\Delta t}(x,t_n) := x - \Delta t u(x,t_n).$$

In practice, we are interested in the value of Y at the mesh-points of an interval $[0,L]$, say x_m, so we use spatial interpolation to compute the terms $Y^n(X_{\Delta t}(x_m,t_n))$ and $\int_{t_n}^{t_{n+1}} f(X_{\Delta t}(x_m,s),s)\,ds$.

Summarizing, we proceed as follows:

- If $X_{\Delta t}(x_m,t_n) \leq 0$ we use the left boundary condition,

$$Y^n(X_{\Delta t}(x_m,t_n)) = Y_{left}(t_n).$$

- Similarly, if $X_{\Delta t}(x_m,t_n) \geq L$ we use the right boundary condition

$$Y^n(X_{\Delta t}(x_m,t_n)) = Y_{right}(t_n).$$

- If point $X_{\Delta t}(x_m,t_n)$ belongs to the interval $[x_{m_1},x_{m_2}] \subset (0,L)$, then

$$X_{\Delta t}(x_m,t_n)) = ax_{m_1} + (1-a)x_{m_2},$$

for some $a \in [0,1]$, and then we take the interpolation

$$Y^n(X_{\Delta t}(x_m,t_n)) = aY^n(x_{m_1}) + (1-a)Y^n(x_{m_2}).$$

References

[1] Statistical review of world energy. 2021, https://www.bp.com/content/dam/bp/business-sites/en/global/corporate/pdfs/energy-economics/statistical-review/bp-stats-review-2021-full-report.pd; 2021.

[2] Renewables 2021. analysis and forecast to 2026. https://iea.blob.core.windows.net/assets/5ae32253-7409-4f9a-a91d-1493ffb9777a/Renewables2021-Analysisandforecastto2026.pdf; 2021.

[3] Bermúdez A, González-Díaz J, González-Diéguez FJ, González-Rueda ÁM. Gas transmission networks in europe: connections between different entry-exit tariff methodologies. Appl Energy 2016;177:839–51.

[4] Azadeh A, Tarverdian S. Integration of genetic algorithm, computer simulation and design of experiments for forecasting electrical energy consumption. Energy Pol 2007;35:5229–41.

[5] Aydin G, Karakurt I, Aydiner K. Analysis and mitigation opportunities of methane emissions from the energy sector. Energy Sources, Part A Recovery, Util Environ Eff 2012;34:967–82.

[6] Aydin G. The application of trend analysis for coal demand modeling. Energy Sources B Energy Econ Plann 2015;10:183–91.

[7] Karakurt İ, Aydin G, Kaya S, Hamzacebi C. Forecasting of Turkey's coal

consumption using grey prediction technique. In: 24th international mining congress and exhibition of Turkey. Turkey: Antalya; 2015. p. 78–82.

[8] Chaczykowski M, Zarodkiewicz P. Simulation of natural gas quality distribution for pipeline systems. Energy 2017;134:681–98.

[9] van der Hoeven T, et al. Gas quality control in simulation. In: PSIG annual meeting, pipeline simulation interest group; 1998.

[10] van der Hoeven T. Math in Gas and the art of linearization. Energy Delta Institute; 2004.

[11] Haeseldonckx D, D'haeseleer W. The use of the natural-gas pipeline infrastructure for hydrogen transport in a changing market structure. Int J Hydrogen Energy 2007;32:1381–6.

[12] Gondal IA, Sahir MH. Prospects of natural gas pipeline infrastructure in hydrogen transportation. Int J Energy Res 2012;36:1338–45.

[13] Schouten J, Michels J, Janssen-van Rosmalen R. Effect of h2-injection on the thermodynamic and transportation properties of natural gas. Int J Hydrogen Energy 2004;29:1173–80.

[14] Tabkhi F, Azzaro-Pantel C, Pibouleau L, Domenech S. A mathematical framework for modelling and evaluating natural gas pipeline networks under hydrogen injection. Int J Hydrogen Energy 2008;33:6222–31.

[15] Hernandez-Rodriguez G, Pibouleau L, Azzaro-Pantel C, Domenech S. Impact of hydrogen injection in natural gas infrastructures. In: Computer aided chemical engineering, vol. 29. Elsevier; 2011. p. 1708–12.

[16] Elaoud S, Hadj-Taïeb E. Transient flow in pipelines of high-pressure hydrogen-natural gas mixtures. Int J Hydrogen Energy 2008;33:4824–32.

[17] Elaoud S, Abdulhay B, Hadj-Taieb E. Effect of hydrogen injection into natural gas on the mechanical strength of natural gas pipelines during transportation. Arch Mech 2014;66:269–86.

[18] Abeysekera M, Wu J, Jenkins N, Rees M. Steady state analysis of gas networks with distributed injection of alternative gas. Appl Energy 2016;164:991–1002.

[19] Hager T, Bentaleb A, Wehrmann E. Simulation system with calorific value tracking for gas distribution grids with an incomplete measurement infrastructure. In: Proceedings of the XX IMEKO world congress. Busan; 2012.

[20] Guandalini G, Colbertaldo P, Campanari S. Dynamic quality tracking of natural gas and hydrogen mixture in a portion of natural gas grid. Energy Proc 2015;75:1037–43.

[21] Guandalini G, Colbertaldo P, Campanari S. Dynamic modeling of natural gas quality within transport pipelines in presence of hydrogen injections. Appl Energy 2017;185:1712–23.

[22] Mikolajková M, Haikarainen C, Saxén H, Pettersson F. Optimization of a natural gas distribution network with potential future extensions. Energy 2017;125:848–59.

[23] Chaczykowski M, Sund F, Zarodkiewicz P, Hope S. Gas composition tracking in transient pipeline flow. J Nat Gas Sci Eng 2018;55:321–30.

[24] Fan D, Gong J, Zhang S, Shi G, Kang Q, Xiao Y, Wu C. A transient composition tracking method for natural gas pipe networks. Energy 2021;215:119131.

[25] Bermúdez A, López X, Vázquez-Cendón M. Finite volume methods for multicomponent euler equations with source terms. Comput Fluid 2017;156:113–34.

[26] Ryan MJ, Mailloux RL, et al. Methods for performing composition tracking for

pipeline networks. In: PSIG annual meeting, pipeline simulation interest group; 1986.

[27] Behbahani-Nejad M, Bermúdez A, Shabani M. Finite element solution of a new formulation for gas flow in a pipe with source terms. J Nat Gas Sci Eng 2019;61:237–50.

[28] Bermúdez A, Shabani M. Finite element solution of isothermal gas flow in a network. J Comput Phys 2019;396:616–52.

[29] Bermúdez A, Shabani M. Modelling compressors, resistors and valves in finite element simulation of gas transmission networks. Appl Math Model 2021;89:1316–40.

[30] Bermúdez A, López X, Vázquez-Cendón ME. Numerical solution of non-isothermal non-adiabatic flow of real gases in pipelines. J Comput Phys 2016;323:126–48.

[31] Osiadacz A. Simulation and analysis of gas network e&fn spon. 1987.

[32] Osiadacz AJ, et al. Different transient flow models-limitations, advantages, and disadvantages. In: PSIG annual meeting, pipeline simulation interest group; 1996.

[33] Banda MK, Herty M. Multiscale modeling for gas flow in pipe networks. Math Methods Appl Sci 2008;31:915–36.

[34] Behbahani-Nejad M, Shekari Y. The accuracy and efficiency of a reduced-order model for transient flow analysis in gas pipelines. J Petrol Sci Eng 2010;73:13–9.

[35] Herrán-González A, De La Cruz J, De Andrés-Toro B, Risco-Martín J. Modeling and simulation of a gas distribution pipeline network. Appl Math Model 2009;33:1584–600.

[36] Herty M, Mohring J, Sachers V. A new model for gas flow in pipe networks. Math Methods Appl Sci 2010;33:845–55.

[37] Grundel S, Jansen L, Hornung N, Clees T, Tischendorf C, Benner P. Model order reduction of differential algebraic equations arising from the simulation of gas transport networks. In: Progress in differential-algebraic equations. Springer; 2014. p. 183–205.

[38] Pambour KA, Bolado-Lavin R, Dijkema G. An integrated transient model for simulating the operation of natural gas transport systems. J Nat Gas Sci Eng 2016;28:672–90.

[39] Gyrya V, Zlotnik A. An explicit staggered-grid method for numerical simulation of large-scale natural gas pipeline networks. Appl Math Model 2019;65:34–51.

[40] Brouwer J, Gasser I, Herty M. Gas pipeline models revisited: model hierarchies, nonisothermal models, and simulations of networks. Multiscale Model Simul 2011;9:601–23.

[41] Papay J. A termeléstechnolǵiai paraméterek változása a gázlelepk müvelese során. OGIL Musz Tud Kuzl; 1968. p. 267–73.

[42] Fang X, Xu Y, Su X, Shi R. Pressure drop and friction factor correlations of supercritical flow. Nucl Eng Des 2012;242:323–30.

[43] Yang X, Zhang S, Zhu W. A new model for the accurate calculation of natural gas viscosity. Nat Gas Ind B 2017;4:100–5.

[44] Dupont T. L^2-estimates for galerkin methods for second order hyperbolic equations. SIAM J Numer Anal 1973;10:880–9.

[45] Penel Y. An explicit stable numerical scheme for the 1 *d* transport equation. Discrete Continuous Dynam Syst 2012;5:641.